

Towards a universal machine learning inter-atomic potential for the $x\text{Li}_2\text{S}-(100-x)\text{P}_2\text{S}_5$ material class

Annäherung an ein universelles Machine Learning Kraftfeld für die $x\text{Li}_2\text{S}-(100-x)\text{P}_2\text{S}_5$ Materialklasse

Wissenschaftliche Arbeit zur Erlangung des Grades
M.Sc.
an der Fakultät für Chemie der Technischen Universität München.

Betreut von Prof. Dr. Karsten Reuter
Lehrstuhl für Theoretische Chemie

Eingereicht von Tabea Huss
80939 München

Eingereicht am München, den 28.1.22

Anhang I

Erklärung

Ich versichere hiermit, dass ich die von mir eingereichte Abschlussarbeit selbstständig verfasst und keine anderen als die angegebenen Quellen und Hilfsmittel benutzt habe.

München, 28.1.22 T.Haj

München, 28.1.22, Unterschrift

List of abbreviations

AIMD	<i>Ab-initio</i> molecular dynamics	ML	Machine learning
AIRSS	<i>Ab-initio</i> random structure search	MSD	Mean square displacement
BCC	Body centered cubic	kPCA	Kernel Principal Component Analysis
DFT	Density functional theory	PES	Potential energy surface
FF	Force field	RMSE	Root Mean Square Error
GAP	Gaussian approximation potential	RSS	Random structure search
GPR	Gaussian process regression	RDF	Radial distribution function
HCP	Hexagonal close-packed	SOAP	Smooth overlap of atomic positions
LPS	Lithium thiophosphate	SSE	Solid state electrolyte
MD	Molecular Dynamics		

Acknowledgements

First of all, thanks to Prof. Dr. Karsten Reuter for the opportunity to do my master thesis in his group. I greatly appreciated the opportunity to join the group seminar and therefore get an overview of the research done in the whole group, which was super insightful. Thanks to Dr. Christoph Scheurer and Dr. Johannes Margraf for welcoming me in their subgroups and for the very helpful and constructive discussions on my thesis. Thanks to Carsten Staacke for being the best supervisor I could have asked for, patiently answering all my questions, giving me a lot of freedom in the meantime, and always being motivated to have a coffee and a nice (off-topic) discussion. Furthermore, I would like to thank Sina Stegmaier, Hanna Türk, Nicolas Bergmann, and Thorben Eggert for providing me with IT support and useful scripts during my thesis. Many thanks to Konstantin Jakob and Patricia König for reading my thesis, patiently correcting unnecessary errors, and their super helpful remarks! Thanks to Maryke Kouyate for cheering me up in the office and giving me the feeling that I am not the only person left on the sixth floor of the yellow tower. Finally, I want to express my gratitude for the endless support from my family and my friends.

Kurzzusammenfassung

Die Materialklasse der Lithiumthiophosphate enthält vielversprechende Kandidaten für die Anwendung als Feststoffelektrolyte in Lithium-Ionen-Batterien. Jedoch sind theoretische *ab-initio* Studien zur Vorhersage von ionischen Leitfähigkeiten, welche aufgrund des hohen Rechenaufwands nur kleine Systemgrößen und kurze Zeitskalen betrachten, auf die realen Materialien nur begrenzt übertragbar. Letztere haben eine komplexe Thiophosphatchemie auf molekularer Ebene sowie Korngrenzen, welche die Materialeigenschaften entscheidend beeinflussen können. Eine Methode mit geringerem Rechenaufwand als *ab-initio* Ansätze, welche dennoch die komplexe Chemie der Materialklasse abbilden kann, wäre demnach erstrebenswert. In dieser Arbeit stellen wir ein universelles atomares Kraftfeld für die Materialklasse vor, welches auf Gauß-Prozess Regression basiert. Das Potential kann kristalline und amorphe Materialien sowie verschiedene molekulare Thiophosphateinheiten beschreiben. Weiterhin wenden wir das Kraftfeld auf eine Reihe von Materialien in der Strukturklasse an, um ionische Leitfähigkeiten und Aktivierungsbarrieren zu bestimmen. Die untersuchten Materialien sind kristalliner (Modifikationen von Li_3PS_4 und $\text{Li}_7\text{P}_3\text{S}_{11}$) und amorpher Natur ($x\text{Li}_2\text{S}-(100-x)\text{P}_2\text{S}_5$, $x = 67, 70$ and 75). Außerdem werden Glass-Keramik-Grenzflächen untersucht.

Die resultierenden Materialeigenschaften sind in guter Übereinstimmung mit Literaturwerten sowohl aus theoretischen als auch experimentellen Studien. Für die amorphen Strukturen wurde explizit der Effekt von verschiedenen molekularen Thiophosphateinheiten und von verschiedenen Li_2S -Prozentsätzen auf die Leitfähigkeit untersucht, wobei für Ersteres kein signifikanter Einfluss gefunden wurde, eine Erhöhung von Letzterem aber die Leitfähigkeit verbessert.

Abstract

The lithium thiophosphate material class provides promising candidates for solid state electrolytes in lithium ion batteries due to high lithium ion conductivities and low material cost. Theoretical *ab-initio* studies probing lithium ion conductivity are constrained in system size and simulated time scales. This limits the transferability of their results to real-world materials in the structure class. Those are characterized by complex thiophosphate microchemistry and grain boundaries influencing the material performance. A method with reduced computational cost, which nevertheless reproduces the material's complex chemistry, would hence be highly desirable. We present the development of a near-universal atomistic potential for the LPS material class employing Gaussian process regression. The atomistic potential can describe likewise crystal and glassy materials and different P-S connectivities (P_mS_n). Furthermore, we apply the ML potential with the aim to probe lithium ion conductivity. The materials studied are crystals (modifications of Li_3PS_4 and $Li_7P_3S_{11}$), glasses of the $xLi_2S-(100-x)P_2S_5$ type ($x = 67, 70$ and 75) and glass-ceramic interfaces.

The obtained material properties for likewise crystals and glasses show a good agreement with results from theory and experiment. For the amorphous materials, the effects of thiophosphate microchemistry and Li_2S content on lithium ion conductivity were explicitly investigated. No influence was found for the former, but ion conductivity increases alongside the latter one.

Contents

1	Introduction	1
2	The LPS material class	3
2.1	Crystalline phases	4
2.2	Glasses and thiophosphate microchemistry	6
2.3	Synthesis strategies	6
2.4	Interfaces	7
3	Chemical machine learning potentials	8
3.1	Replacing <i>ab-initio</i> methods by force-field approaches	8
3.2	Gaussian process regression: an overview	8
3.3	Description of atomic neighborhoods	9
3.4	The GAP framework	11
3.5	A measure for the similarity of chemical structures	12
4	Computational details	14
5	Adjusting the ML potential to the system	16
5.1	Choice of initial model and hyperparameters	16
5.2	Training of crystal structures	17
5.3	Training of amorphous structures	19
5.4	Training of further microchemistry: $P_2S_6^{4-}$	22
5.5	Random structure search	25
5.6	Thoughts on training of extended systems	29
6	Results from system characterization using the ML interatomic potential	30
6.1	Crystal	31
6.2	Glass	34
6.2.1	Chemical reasonability and microchemistry	35
6.2.2	Conductivity	37
6.3	Interface	41
6.3.1	Building and sintering	41
6.3.2	Characterization	41
6.3.3	Conductivities	45
7	Conclusion and outlook	47

8 Appendix	49
8.1 FF Training	49
8.2 Molecular Dynamics	52
List of Figures	56
List of Schemes	58

1 Introduction

While lithium-ion batteries with liquid electrolytes entered the market in 1991, all-solid-state lithium-ion batteries (ASS-LIB), although investigated for decades, are still not widely applied. They promise several advantages in comparison to liquid electrolyte batteries. The liquid electrolytes in conventional lithium-ion batteries are easily flammable, raising doubts about their suitability in terms of operation safety for electric mobility. Solid electrolytes in contrast are inflammable. Longer lifetimes due to less degradation of the battery have also been shown.[1, 2] With further advances in the ASS-LIB field solid state batteries may potentially feature a lithium metal electrode, thus increasing in energy density and outperforming conventional lithium ion batteries.[1]

Solid electrolytes of the LPS (Lithium thiophosphate) material class have gained substantial attention in the literature due to their favorable properties.[3] First, they possess high conductivities of up to 10^{-2} S/cm, which ranks them among the most conductive solid electrolytes known at present like $\text{Li}_{10}\text{GeP}_2\text{S}_{12}$ or $\text{Li}_{1.3}\text{Al}_{0.3}\text{Ti}_{1.7}(\text{PO}_4)_3$. [4, 5] Secondly, they are composed of the earth-abundant elements sulfur and phosphorous, which would allow for applications at large scales.

However, the design of a potent solid electrolyte in this material class is hampered by the poor understanding of structure-property relations in the material class. This is manifested by huge deviations in reported conductivity from theory and experiment.

As such, $\beta\text{-Li}_3\text{PS}_4$ serves as an illustrating example. Experimental studies report a lithium ion conductivity of approximately 10^{-7} S/cm, which makes the material unsuitable for real-world battery applications.[6] An *ab-initio* study however predicts a conductivity of 10^{-1} S/cm, which implies a deviation of six orders of magnitude from the experimental values and would make the material the new record holder in solid-state lithium ion conduction. [7] These huge discrepancies might be attributable to computational limitations of the *ab-initio* methods, which constrain the description both in system size (studied systems are typically composed of no more than 100 atoms) and simulated time (typical AIMD (*Ab-initio* molecular dynamics) runs rarely exceed 50 ps).[8, 9] The problem is fortified by the complex nature of materials in the structure class, where pure glassy or crystalline materials do not occur and boundary regions have a decisive influence on lithium ion conduction.[10, 11] System sizes of several thousand atoms are required to describe such complex systems, which is out of reach for DFT (Density functional theory) approaches. $\text{Li}_7\text{P}_3\text{S}_{11}$ is exemplary as it is usually obtained via a ball milling routine yielding a glass-ceramic structure.[12–14] Moreover, glassy materials, even though lacking reflexes in X-ray diffraction analysis, are found to contain small crystal precipitations.[15] Furthermore, a large structural variability on a molecular level, more precisely different thiophosphate building blocks, is found in the amorphous materials and a proper assessment of their performance would require statistical ensembles.[3, 16]

The approach taken in this work suggests to replace *ab-initio* methods to study the materials by kernel-based forces fields (FFs), which reduces the computational cost by a factor of > 1000 . This cost reduction allows for an upscaling of both time- and size scale: Molecular dynamics simulations with lengths of several nanoseconds and system sizes of several thousand atoms become feasible. Furthermore, the flexibility offered by an ML (machine learning) approach allows to implement a FF which is more versatile and can better represent the occurring complex chemistry than classical force field approaches at present.[17]

This work is split into two parts: First, the extension of an already available ML force field to yield a universal description of the LPS material class. Second, the application of the FF to selected compounds in the material class to validate the FF and the long-term goal to try to find systematic structure-property relations. This might facilitate the design of potent LPS solid electrolyte from an experimental point of view.

2 The LPS material class

In this section, the literature of the lithium thiophosphate material class is discussed. LPS is of particular interest as a potential solid-state electrolyte (SSE), as two favorable properties arise from the chemical nature of LPS. First, high lithium ion conductivities of $\sigma > 10^{-4} \text{ S cm}^{-1}$ enable fast charging and discharging in SSE. Second, and of special interest from an environmental perspective, LPS consists of cheap and earth-abundant materials. The chemical nature of lithium thiophosphate solid materials can be broken down to lithium being the mobile species and a set of thiophosphate polyhedra forming an immobile structural matrix. Thiophosphate polyhedra are visualized in Figure 1. Among these, the simplest thiophosphate building block is a monomer tetrahedron (*ortho*-thiophosphate, a)). More complex chemistry occurs when considering dimeric polyhedra: Two corner-linked monomers sharing one sulfur atom (*pyro*-thiophosphate, b)) are the second most common building blocks. Furthermore, dimers with a direct P-P bond exist (*hypo*-thiodiphosphate $\text{P}_2\text{S}_6^{4-}$, c)). Those are stabilized by the lower oxidation number (+4) on phosphorous. The building block with identical elemental composition but an oxidation number of +5 on phosphorous (*meta*-thiodiphosphate, d)) is composed of two edge-linked PS_4 tetrahedrons. Finally, longer corner-linked chains (*meta*-thiophosphate, e)) are found in the material class.[3]

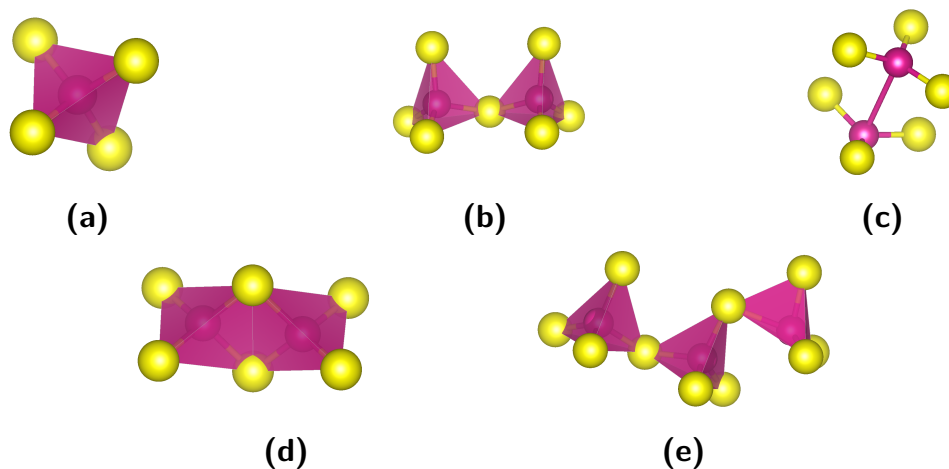


Figure 1: P-S microchemistry contained in the $x\text{Li}_2\text{S}-(100-x)\text{P}_2\text{S}_5$ material class. a) *ortho*-thiophosphate PS_4^{3-} , b) *pyro*-thiophosphate $\text{P}_2\text{S}_7^{4-}$, c) *hypo*-thiodiphosphate $\text{P}_2\text{S}_6^{4-}$, d) *meta*-thiodiphosphate $\text{P}_2\text{S}_6^{2-}$, e) *meta*-thiophosphate chain $(\text{PS}_3^-)_n$. [3]. Phosphorous is displayed in violet, sulfur in yellow.

2.1 Crystalline phases

Li_3PS_4 is probably the most commonly studied compound in the ternary Li-P-S phase diagram. Three different crystal phases are found for this stoichiometry: α , β and γ . All these phases solely contain the simple monomer building block (PS_4^{3-}). While $\gamma\text{-Li}_3\text{PS}_4$ is stable at room temperature, two phase changes are observed at higher temperatures. A first phase change occurs at around 600 K (γ to β), followed by a transformation at roughly 800 K (β to α).[18]

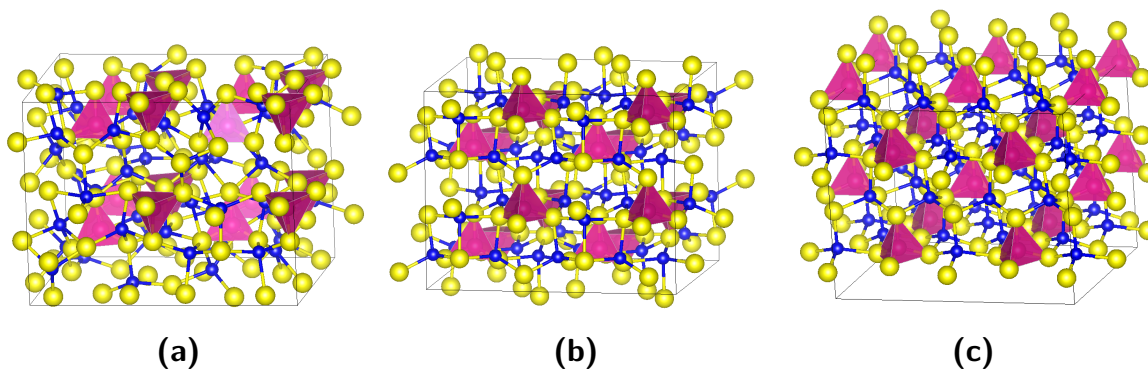


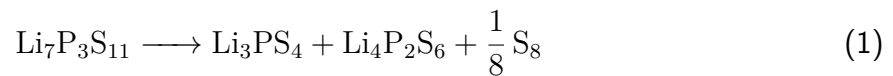
Figure 2: Crystal phases of Li_3PS_4 a) $\alpha\text{-Li}_3\text{PS}_4$ b) $\beta\text{-Li}_3\text{PS}_4$ c) $\gamma\text{-Li}_3\text{PS}_4$. The γ -phase is the stable one at room temperature, which exhibits a phase change to the β -phase at 500-700 K. Lithium is displayed in blue, phosphorous in violet, and sulfur in yellow.

The α -phase is of less importance for battery applications as it is not stable at operating temperatures, whereas the β -phase can occur at room temperature e.g. stabilized by small stoichiometric changes.[19] Conceptually, the three phases can be distinguished by their different arrangement of PS_4^{3-} apexes, which are either all pointing in the same direction (γ) or arranged in a zig-zag fashion in one (α) or two directions (β). As a direct consequence, the coordination numbers of lithium ions differ between the two crystal phases: In case of the γ -phase, lithium ions are tetrahedrally coordinated by sulfur but partially tetrahedrally and octahedrally in the β -phase.[18]

Low room temperature (RT)-conductivities of 2.6×10^{-7} and $9.0 \times 10^{-7} \text{ S cm}^{-1}$ are experimentally reported for the β - and γ -crystals.[18] However, the conductivity of Li_3PS_4 is strongly increased in glass-ceramic materials of the β -phase. Glass-ceramics are experimentally prepared by embedding the crystal phase in an amorphous matrix, reaching values of approximately $1 \times 10^{-4} \text{ S cm}^{-1}$. [10, 20]

Complex thiophosphate compounds can be found in crystal structures of other stoichiometries such as $\text{Li}_4\text{P}_2\text{S}_6$ (composed entirely of $\text{P}_2\text{S}_6^{4-}$ units) and $\text{Li}_7\text{P}_3\text{S}_{11}$ (composed of PS_4^{3-} and $\text{P}_2\text{S}_7^{4-}$ in a ratio of 1:1). $\text{Li}_4\text{P}_2\text{S}_6$ on one hand exhibits conductivities of $\leq 1 \times 10^{-6} \text{ S cm}^{-1}$ rendering it unsuitable for application in all-solid-state lithium-ion battery applications.[21]

$\text{Li}_7\text{P}_3\text{S}_{11}$ on the other hand is a promising candidate for SSE, as it offers an exceptional conductivity in the range of 1×10^{-3} to $2 \times 10^{-2} \text{ S cm}^{-1}$ at room temperature and low activation barriers of approximately 0.2 eV.[11, 22, 23] An even higher conductivity of $5.6 \times 10^{-2} \text{ S cm}^{-1}$ is predicted by AIMD simulations. This difference between AIMD and experimental lithium ion conductivities is assumed to be due to grain boundaries inhibiting synthesized materials to reach the high bulk conductivity of the crystal.[23] Lithium ions in the $\text{Li}_7\text{P}_3\text{S}_{11}$ crystal are exclusively tetrahedrally coordinated and the proposed conductivity mechanism is a collective motion of lithium ions across empty tetrahedral sites.[23] However, the thermal stability of the phase is limited (an energy above-hull of 27 meV/atom is predicted[23]) and the following decomposition occurs already at temperatures of around 600 K:



Hence, the annealing of glassy materials to yield the crystal is challenging and the material is usually obtained as a glass-ceramic. [12–14]

Both Li_3PS_4 and $\text{Li}_7\text{P}_3\text{S}_{11}$ do not possess a sufficient electrochemical window to be stable in contact with a lithium metal, which leads to the formation of a protective boundary layer, possibly degrading the ion conductivity.[7, 11]

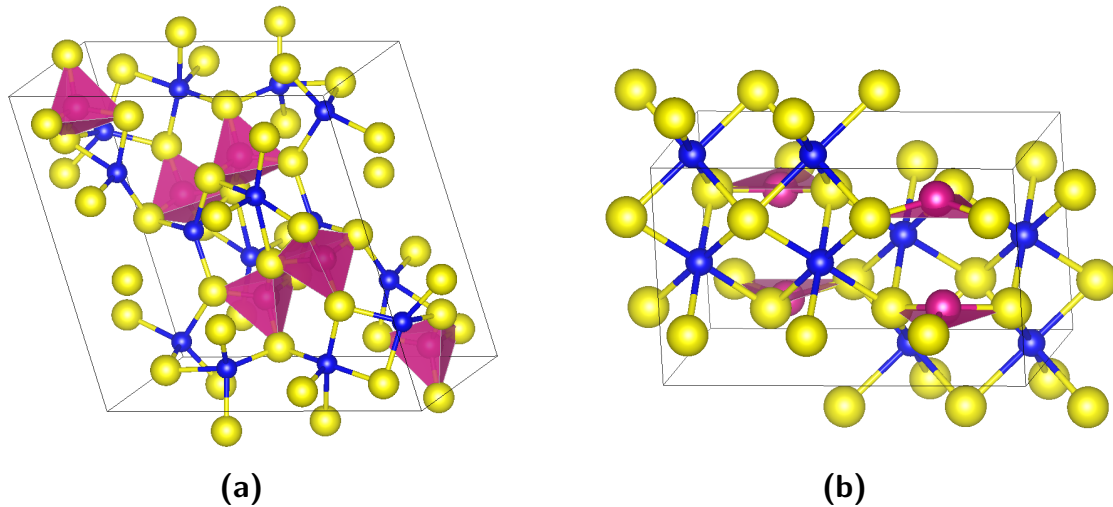


Figure 3: Further crystal structures existing in the ternary Li-P-S system. a) The metastable $\text{Li}_7\text{P}_3\text{S}_{11}$ crystal, which contains in a ratio of 1:1 PS_4^{3-} and $\text{P}_2\text{S}_7^{4-}$ building blocks. b) $\text{Li}_4\text{P}_2\text{S}_6$, containing exclusively $\text{P}_2\text{S}_6^{4-}$ building blocks. Lithium is displayed in blue, phosphorous in violet, and sulfur in yellow.

2.2 Glasses and thiophosphate microchemistry

While LPS crystals have fixed stoichiometries and P-S chemistry, high structural variability is found in LPS glasses. The plasticity arising from the amorphous nature of the glasses makes them more robust to mechanical stress, exerted by volume changes during cell cycling.[1] Amorphous structures of $x\text{Li}_2\text{S}-(100-x)\text{P}_2\text{S}_5$ (x representing the Li_2S atom percentage) are examined in a range of $60 < x < 80$. [16] Depending on the choice of x , different polyhedron compositions are obtained. In general, four of the five thiophosphate substructures are found in quantitative ^{31}P magic angle spinning nuclear magnetic resonance and Raman experiments. [16, 24, 25] $\text{P}_2\text{S}_6^{2-}$ is the only microstructure which is not identified experimentally in the amorphous structures. While the other species occur in smaller concentrations, the chemistry is dominated by the PS_4^{3-} and $\text{P}_2\text{S}_7^{4-}$ components. The ratio between the former and the latter one depends on the choice of x in the stoichiometry: At low Li_2S content ($60 \leq x \leq 70$), the dominating species is $\text{P}_2\text{S}_7^{4-}$, whereas mainly single tetrahedrons are found for $75 \leq x \leq 80$. The content of $\text{P}_2\text{S}_6^{4-}$ polyhedrons is strongly dependent on the method of synthesis: a ball-milling approach yields the $\text{P}_2\text{S}_6^{4-}$ polyhedron to make up approximately 10 % of the phosphorous content in the material independent of Li_2S content. A microwave-assisted synthesis strategy does not find any contribution at room temperature. [16, 24, 25] PS_3^- chains are only found for $x = 60$. [16]

The ion conduction mechanism in the glassy structures fundamentally differs from the one found in their crystal counterparts: For Li_3PS_4 , a so-called paddlewheel effect has been found by first-principle calculations, where lithium migration is facilitated by the rotation of thiophosphate polyhedra, which is observed even at room temperature. [26]

The conductivities of amorphous LPS compounds generally lie in the range of 10^{-5} to $10^{-4} \text{ S cm}^{-1}$, which makes them less conductive than the $\text{Li}_7\text{P}_3\text{S}_{11}$ crystal, but significantly more conductive than the Li_3PS_4 phases. [8, 16, 20, 27] Furthermore, the conductivity tends to rise with increasing Li_2S content. [16] However, systematic studies of 1) how the microchemistry is influenced by the synthesis conditions and 2) how the microchemistry influences the observed lithium ion conductivity have not yet been performed but would be highly desirable for a better understanding of the material class.

2.3 Synthesis strategies

Three main strategies are employed for the synthesis of compounds in the LPS material class: solid-state reactions, ball-milling, and wet-chemical methods. Materials obtained by ball-milling are amorphous and need to be annealed to obtain crystals or glass-ceramics. Ionic conductivities strongly depend on the synthesis strategy, e.g. the $\text{Li}_7\text{P}_3\text{S}_{11}$ crystal with the

highest conductivity in the literature was obtained via solid-state reactions, while the conductivity of β - Li_3PS_4 was highest when synthesized via a wet-chemistry route.[3, 22, 28]

2.4 Interfaces

Examining only the separate crystalline and glassy phases cannot explain the conductivities in experimental samples. Those are in general either microcrystalline or glassy with small crystalline subdomains. In the case of Li_3PS_4 , the conductivity has been found to substantially increase in a microcrystalline sample in comparison to the pure crystal.[15] For $\text{Li}_7\text{P}_3\text{S}_{11}$, the conductivity is decreased by higher degrees of amorphization but the formation of glass-ceramics is nevertheless unavoidable due to the poor stability of the crystal.[27]

Studies examining the two-dimensional interface emerging from the contact of a glassy- and a crystalline material are barely existent in the literature, as they are not well-accessible by experiment. Tsukasaki *et al.* were the first to directly study glass-ceramic structures of Li_3PS_4 via transmission electron microscopy and X-ray diffraction, which allowed them to identify the dominant crystal phase (β) and its exposed surface ($\bar{1}10$).[15] Only one theoretical study exists for the same stoichiometry, where the diffusion across a glass-ceramics interface of γ Li_3PS_4 is studied with a classical force field, yielding ionic conductivities bridging those of the crystalline and amorphous compounds. However, the study is limited to the (100) surface and the γ -phase, without experimental evidence that those are dominantly occurring in glass-ceramics.[17]

3 Chemical machine learning potentials

3.1 Replacing *ab-initio* methods by force-field approaches

When trying to obtain material properties like e.g. lithium ion conductivities from simulation, these properties usually need to be determined using large supercells and long molecular dynamics (MD) runs.

Density functional theory (DFT) is the state-of-the-art method in computational chemistry, which can provide highly accurate energies and forces of a system. These further enable the propagation of the system in time. However, simulation times and system sizes are strongly limited by the high computational cost of the method. This cost is caused by solving the complete quantum mechanical problem to obtain the desired energies and forces. Force field approaches aim to serve as surrogate models, which ignore the electronic problem and solely describe the energy and forces resulting from the latter one as a function of atomic coordinates, yielding an approximated potential energy surface (PES).

Recently, ML methods are receiving increasing attention in the field of computational chemistry, more and more replacing classical force fields. To briefly clarify the difference between machine learning-based methods and classical fitting: Both aim to find a fitting function $\tilde{y}(x)$ (also called predictor in machine learning jargon) of certain input values x (features/descriptors, some representation of atomic coordinates) to approximate the target function $y(x)$ (total energy, forces and other system properties from *ab-initio* methods like DFT). To reach this goal both approaches minimize the error, quantified by a penalty function, between the predictor function and $y(x)$, using a specific set of data points from the function $y(x)$. For the minimization of the error a set of coefficients c_m , which are part of the predictor function, is tuned.

However, in classical force fields the predictor takes a predefined, fixed functional form, which is often inspired by physical reasoning (e.g. includes terms like a Van-der-Waals potential). No functional form is predefined in the case of machine learning, the functional form closely depends on the provided data set. Thus machine learning models have an advantage over classical force fields in their high degree of flexibility, at the cost of potentially losing their physical interpretation.

3.2 Gaussian process regression: an overview

A variety of attempts at GPR explanation exist. Here, the weight-space view recently introduced in a review by Csanyi *et al.* is favored and used.[29] GPR can be interpreted as a

Kernel-based approach, where the regressor is simply a sum over M Kernel basis functions $k(x, x_m)$, which are weighted by the fitting coefficients c_m :

$$y(x) = \sum_{m=1}^M c_m k(x, x_m) \quad (2)$$

The basis functions can be intuitively understood as a similarity measure between the input descriptor x and the descriptor x_m of the corresponding basis function. They take different functional forms such as a Gaussian function or a simple scalar product. It is important to note that M does not coincide with the number of training points N used to fit the model: in the case of sparse GPR, the number of training points is reduced to a representative set to make the computational demand of the model independent of the training set size.

To find the fitting coefficients c_m , a loss function is defined:

$$L = \sum_{n=1}^N \frac{[y_n - y(x_n)]^2}{\sigma_n^2} + R. \quad (3)$$

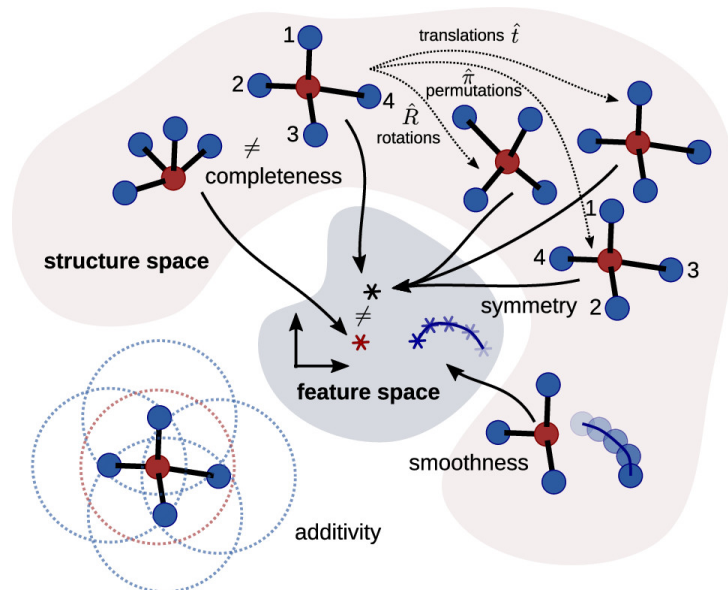
The relative importance of every individual data point is expressed by σ_n . Furthermore, a regularization term R (employing Tikhonov regularization) introduced into the model, which aims to prevent overfitting and to account for the uncertainty of the input data. An analytic expression for the coefficients can then be obtained by differentiating and solving for the coefficient vector c :

$$c = (K_{MM} + K_{MN}\Sigma^{-1}K_{NM})^{-1}K_{MN}\Sigma^{-1}y. \quad (4)$$

Σ is a diagonal matrix of σ_n^2 values, K_{NM} is the Kernel matrix ($[K_{NM}]_{nm} = k(x_n, x_m)$) and y is the vector of output data.

3.3 Description of atomic neighborhoods

When applying Gaussian process regression to molecular structures, a reasonable metric for the definition of the descriptor variables is needed. This is a non-trivial task, as the descriptor needs to fulfill a set of requirements (summarized in Figure 1) which make obvious choices like atomic coordinates unsuitable to the problem. Firstly, the description needs to be complete, meaning that it provides a unique description for a chemical structure. Secondly, it should reproduce the totally symmetric behavior of the Hamiltonian and the total energy of the system. Consequently, invariance with respect to rotations, translations, and permutations of equivalent atoms is requested. Furthermore, the descriptor should be smooth: a continuous structural change should also be continuous in feature space. The final criterion of additivity requests that property predictions based on the descriptors are not system-size dependent.[30]



Scheme 1: Summarized properties which are demanded for metrics describing chemical environments: Additivity, invariance with respect to rotation, translation and permutation, completeness and smoothness. Reprinted with permission from Deringer *et al.*[29] Copyright 2021 American Chemical Society.

A straightforward description of chemical structures which is routinely employed in classical force fields would be a simple element-dependent pair distance:

$$r_i - r_j = r_{ij}. \quad (5)$$

Potentials can then be built by summation over all possible atom pairs:

$$E = \sum_{i,j} V(|r_i - r_j|) = \sum_{i,j} V(r_{ij}). \quad (6)$$

While this description is translationally, rotationally, and permutationally invariant, simple and intuitively to implement, it is evident that it is not able to represent the complexity of a chemical system. The description can be improved by adding a three-body, or even higher-order representations.[31]

A different approach aims at defining one single local multi-body metric for every atom in the structure. A popular descriptor that follows this approach and fulfills the aforementioned criteria is the Smooth overlap of atomic positions (SOAP).[32] SOAP combines the definition of the metric with the similarity measure from the beginning. It defines the similarity measure as an inner product of atomic neighbor densities:

$$S(\rho, \rho') = \int \rho(\mathbf{r})\rho'(\mathbf{r})d\mathbf{r}. \quad (7)$$

The atomic neighbor density $\rho^{i,a}(r)$ of an atom i of species a is defined as:

$$\rho^{i,a}(\mathbf{r}) = \sum_j \delta_{aa_j} \exp\left[\frac{-|\mathbf{r} - \mathbf{r}_{ij}|^2}{2\sigma_a^2}\right] f_{cut}(r_{ij}). \quad (8)$$

Per definition, the neighbor densities are local quantities, since contributions past a cutoff radius r_{cut} are suppressed by a smooth function f_{cut} ($r_{ij} = 0$ for $r_{ij} > r_{cut}$). The hyperparameter σ_a is introduced into the model, which describes the width of the Gaussians placed at the atomic neighbor positions and hence the smoothness of the model. The resulting Kernel functions are already permutationally, yet not rotationally invariant. To define a Kernel function that fulfills this criterion the Gaussian functions from Equation 8 are developed in a basis of radial functions and spherical harmonics:

$$\rho^{i,a}(\mathbf{r}) = \sum_{nlm} c_{lm}^i(r) \cdot R_n(r) Y_{lm}(\hat{\mathbf{r}}) \quad (9)$$

Two further hyperparameters are introduced into the model by expansion: the radial cutoff n and the angular cutoff l , which should be chosen large enough to yield reasonable errors. The final SOAP descriptor (also called the Power Spectrum) is then obtained by symmetrization of the coefficients $c_{nlm}^{i,a}$:

$$p_{nn'l}^{iaa'} = \frac{1}{\sqrt{2l+1}} \sum_m (c_{nlm}^{ia})^* c_{n'lm}^{ia'}. \quad (10)$$

3.4 The GAP framework

The GAP (Gaussian approximation potential) framework is essentially the application of GPR in the field of interatomic potentials (implemented in the QUIP code)[33] to calculate the total energy, forces, and various other fitting parameters like Virials from an input geometry represented by a local descriptor. The question directly emerges of how to calculate a global property like the total energy from the local descriptor description. In the GAP framework, this problem is approached by expressing the total energy as a sum of local contributions ϵ from N atoms, where q_i^n denotes the local geometry representation:

$$E \approx E_{short} = \sum_n \epsilon(q_1^{(n)}, \dots, q_M^{(n)}). \quad (11)$$

Consequently, the energy in the GAP approach is a local quantity, neglecting the long-range contribution of the energy and introducing a so-called locality error into the model. It dictates a lower boundary for the accuracy reachable by the model.[34]

As the local energy is not directly accessible from reference methods like DFT, a formulation to fit such properties is needed. Furthermore, different properties like forces and energies need

to be determined in the same procedure. A linear operator \hat{L} , which is applied to the estimator $y(x_i)$, yielding the accessible fitting property $Y(x_i)$, provides a solution to both problems.[34] Concerning the representations discussed in Section 3.3, a combination of different descriptors is commonly used, which has the advantage that different chemical regimes can be described with variable precision, e.g. by approximately describing a repulsive short-range regime using a two-body descriptor and the attractive regime with higher precision using the SOAP descriptor. The energy expression from Equation 2 is then separated in two parts which are weighted by coefficients (δ_2 for two-body and δ_{MB} for many-body representation) and yields two sets of fitting coefficients ($c_{2,m}$ and $c_{MB,m}$). M_2 and M_{MB} denote the respective number of sparse points, ξ_i and ξ_m the normalized SOAP vectors.[29]

$$E = \sum_{ij} \delta_2^2 \sum_{m=1}^{M_2} c_{2,m} e^{\frac{|r_{ij}-r_m|^2}{2\theta^2}} + \sum_i \delta_{MB}^2 \sum_{m=1}^{M_{MB}} c_{MB,m} k(\xi_i, \xi_m) \quad (12)$$

3.5 A measure for the similarity of chemical structures

The SOAP descriptor has not only proven suitable as descriptor for the GAP framework, but is also becoming increasingly popular as a metric for the similarity of local and global structures.[35, 36]

From a set of local structures, the Kernel matrix of SOAP descriptors can be evaluated. It is composed of entries K_{ab} describing the similarity of two local environments a and b , and further yielding a value between 0 and 1. The Kernel is defined as a power of a dot product:

$$K_{a,b} = (\xi_a \cdot \xi_b)^\zeta \quad (13)$$

with ζ being the expansion coefficient. The following metric to convert the similarity into a distance measure has been proposed: [36]

$$D = \sqrt{2 - 2k(\xi, \xi')}. \quad (14)$$

An identical approach can be used to obtain a global similarity of whole structures A and B, with the difference that a *global* SOAP descriptor needs to be defined first. This is achieved by averaging the expansion coefficients c_{nlm}^{ia} of the power spectrum (Equation 10):

$$\bar{c}_{nlm}^i = \frac{1}{N} \sum_{a \in A} c_{nlm}^{ia}. \quad (15)$$

Multiple reduction techniques (e.g. Kernel Principal Component Analysis (kPCA) or multi-dimensional scaling)[30, 35] have been successfully employed to reduce the dimensionality of local or global similarity Kernels, which allows to visualize them in a more intuitive two-

dimensional space. kPCA, which is the method used in this work, is an extension of conventional PCA. PCA is a method to transform the data into a coordinate system, with axes derived from the maximization of variance along the axes. These are then sorted by data variance. To display a presentation of the data on a 2D map, the first two principal components can be selected. PCA can only separate linearly separable data, whereas kPCA introduces a non-linear separability by transforming the data x into a higher-dimensional feature space $\phi(x)$. No calculations are explicitly conducted in the high-dimensional feature space, as a Kernel (e.g. a dot product or Gaussian) is calculated from $\phi(x)$ and the following decomposition is then conducted utilizing this Kernel. [37]

4 Computational details

Ab-initio calculations *Ab-initio* single-point calculations were performed using the FHI-aims package. The PBE exchange-correlation functional from the GGA family, using 'light' default integration grids, and the "tier 1" basis set of numerical atomic orbitals was chosen.[38, 39] The Brillouin zone was sampled using one k-point.

Initial geometries for the utilized crystals were taken from the Materials Project database,[40] apart from the γ - and the α -Li₃PS₄ crystal, which were not available there and therefore taken from literature.[9, 18] The structure of the α -crystal in literature was found to be lithium deficient, the correct stoichiometry was obtained by sampling additional lithium ions using a Voronoi Tessellation of the thiophosphate grid.

GAP The GAP plugin to the QUIP code was used to perform force field fits.[33] The technical hyperparameters for the GAP are discussed in Section 5.1.

Molecular dynamics MD simulations were conducted utilizing LAMMPS[41] linked with the QUIP package, employing a time step of 2 fs throughout.[32] For the trajectories in an NVT ensemble, the Nosé-Hoover thermostat was used in combination with a damping parameter of 2 ps.[42]

For the MD runs of crystal structures, supercells were utilized, hosting 256 atoms for α -Li₃PS₄ (2x2x2 supercell), 128 atoms for β - and γ -Li₃PS₄ (2x2x1 supercell) and 336 atoms for Li₇P₃S₁₁ (2x2x2 supercell). For the conductivity analysis, production geometries were equilibrated in the NVT ensemble for 100 ps, followed by a 3 ns production step, using the NVE ensemble.

Structure generation and data analysis Amorphous geometries were generated using Python 3.8 and the Atomic Simulation Environment (version 3.22.0).[43] To evaluate forces and energies and locally optimize geometries, the Quippy package was used.[33] A maximum force of 3 eV Å⁻¹ was employed and the Broyden-Fletcher-Goldfarb-Shanno algorithm was used for minimization.

The Voronoi Tessellation was performed via the `scipy.spatial` Python module which is based on the Qhull library.[44] Clustering of points was done with the use of the k-Means algorithm implemented in the `sklearn.cluster` Python module.[45] Radial distribution functions (RDF) were partially calculated utilizing the `get_rdf` function from `ase.Analysis` and for the partial RDFs using an implementation already available in the group. The degree of amorphization

was determined using a Fourier transform-based implementation also available in the group.[46]
All geometries were visualized utilizing Vesta.[47]

Similarity analysis Similarity analysis was conducted utilizing the python package DScribe[48] and the SOAP parameters which were used in the force field.

The global similarity analysis was done by using the Quippy and the *average*-option in the SOAP descriptor module.[33]

2D maps were created by plotting the first two principal components of a kPCA decomposition, which utilized a polynomial Kernel.

Random structure search To conduct a fully randomized search of the potential energy surface, the *Ab-initio* random structure search (AIRSS) program was utilized.[49] An initial number of 10000 structures were generated, using one to three stoichiometries of Li_3PS_4 and the *symmops*=1-8 option. Initial bond length parameters of 2.4 - 3.0 Å for lithium, 1.8 - 2.05 Å for phosphorous and 1.8 - 2.3 Å for sulfur were used. These values were determined by extracting distances from the crystal structures and adding tolerance in both directions. An average volume of 20 \AA^3 was used for all three atom types, which was obtained by taking the density of the crystal and dividing it by the total number of atoms. From the 10000 initial stoichiometries the 30 most dissimilar ones were selected by farthest point sampling using the Kernel matrix of global descriptors and the same SOAP parameters as employed for the force field (see Table 1).

5 Adjusting the ML potential to the system

The aim of this section is to describe a training protocol that can be used to fit a GAP model to the LPS material class. Ideally, the desired force field provides a universal description of the LPS class. Hence, it should be able to describe different types of materials (crystals, glasses, interfaces) and P-S microchemistries (e.g. PS_4^{3-} , $\text{P}_2\text{S}_7^{4-}$, $\text{P}_2\text{S}_7^{4-}$), which makes it superior to classical force fields presented in the literature, since those are limited to e.g. the PS_4^{3-} moiety.[17] To obtain such an FF, training geometries have to be selected accordingly. In this work the following training philosophy is used: In a stepwise approach first crystal structures (Section 5.2), then amorphous structures (Section 5.3), and then structures with a more complex microchemistry (Section 5.4), and finally structures obtained from random structures search (Section 5.5) are introduced. Furthermore, it would be desirable to train the FF for interfacial structures, which is not performed in the current work, yet discussed in Section 5.6.

5.1 Choice of initial model and hyperparameters

As an initial model, a GAP based on a combined two-body and SOAP representation is used, yielding an energy expression as shown in Equation 12. The model is trained on energies and forces, tensorial stress contributions are not taken into account. An initial training set and trained GAP potential is already available from previous work,[50] which includes crystals and glassy structures for the stoichiometry $\text{Li}_7\text{P}_3\text{S}_{11}$. Additionally, a set of initial hyperparameters is inherited from the available FF and provided to the model. These are given in Table 1. The number of sparse points and the gaussian width have been determined by a cross validation combined with a grid search, cutoff radii are taken from a locality test.[51] Remaining parameters are specified by using heuristics from literature.[29]

Table 1: Technical hyperparameters for two-body- and SOAP descriptors and regularization.

parameter	two-body	SOAP
r_{cut}	5.5 Å	6.0 Å
$n_{sparsepoints}$	20	2000
sparification method	uniform	CUR decomposition
σ_a		0.7 Å
$[l_{max}, n_{max}]$		[3,9]
ζ		2
σ_{reg}	0.01 eV/atom, 0.1 eV Å ⁻¹	

The applied model is intrinsically charge-free. A GAP including electrostatic contributions and thus minimizing the locality error has been developed in the group, but it has been proven to offer only negligible improvements unless studying non-isotropic environments. Furthermore, electrostatics in the LPS material class are difficult to implement, as different oxidation states are observed especially for sulfur.[51]

5.2 Training of crystal structures

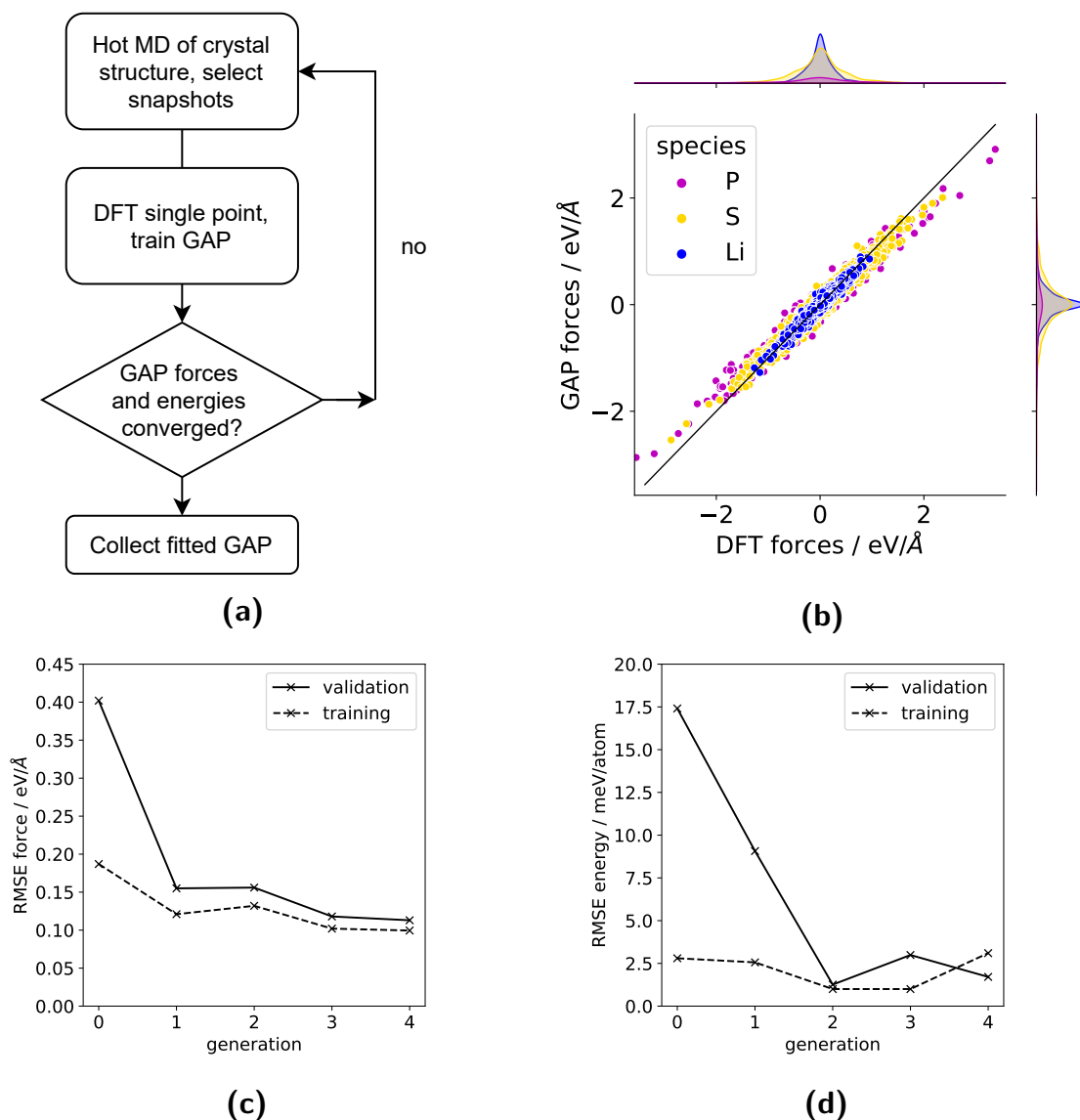


Figure 4: a) Workflow for the iterative training approach of crystalline structures. Hot MD snapshots ($T = 600$ K) are added to the force field training set until a convergence of force and energy RMSEs is approached. b) Force correlation for the final validation set. c) Force RMSEs and d) Energy RMSEs for the iterative training. Final RMSEs are approximately $0.1 \text{ eV } \text{Å}^{-1}$ and 2.5 meV/atom .

The first structure class with which the existing training set is aimed to be enhanced are Li_3PS_4 crystals. As explained in Section 2.1, three modifications exist for this stoichiometry, namely α , β , and γ . The force field is only trained on crystal structures from the β -modification. This is motivated by the fact that all modifications contain the same thiophosphate building block and have very similar RDFs. We therefore use the α - and γ -modifications as an additional validation of the FF (see Figure 22 in the Appendix). Similar force RMSEs are found for those. An energy offset occurs, but the relative energy prediction within the sample sets is still very good.

To add representative training configurations to the training set, several things need to be considered. First, the training configurations should be low in energy, but also represent local minima of the PES energetically slightly higher than the global minimum. Those can be expected to be populated during a molecular dynamics run. A trivial, yet computationally demanding, possibility to obtain those configurations would be an *ab-initio* molecular dynamics run. However, the available force field is already trained on configurations of the $\text{Li}_7\text{P}_3\text{S}_{11}$ crystal, showing near-DFT accuracy. Hence, the force field itself can be used to generate fitting configurations. Yet, it should be expected that the force field, which is not yet converged on the respective structure class, might drift away from the regions of the potential energy surface which would be populated during AIMD runs. Consequently, a self-consistency approach is proposed: Initially, the current force field is used to produce short MD trajectories, from which snapshots are selected and added to the training set. The GAP FF is then retrained with the updated training set. Finally, the performance (root mean square error (RMSE) of forces and energies per atom, using DFT values as a reference) of the old and newly-generated force field is then tested on the set of snapshots. This procedure is iteratively repeated until the energy and force RMSEs have converged. Different strategies like farthest point sampling might be employed to select representative structures from the MD runs, however, a straightforward, randomized approach is tested first and proves to converge the FF in five generations. The iterative training cycle is visually displayed in Figure 4a and the force - and energy RMSEs are shown in Figure 4c and d. Forces and energies converge at RMSEs of $0.1 \text{ eV}/\text{\AA}$ and $2.5 \text{ meV}/\text{atom}$, respectively.

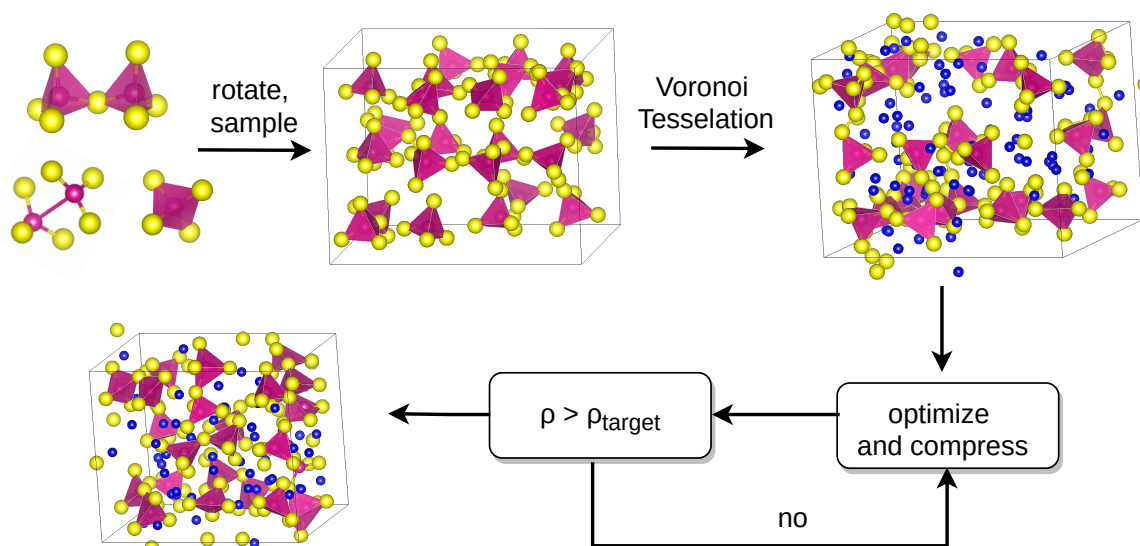
5.3 Training of amorphous structures

Sampling approach

To build amorphous counterparts for the crystalline structures, a Monte Carlo-like sampling approach is chosen. This approach allows, contrary to a melt-quench approach, for the free tuning of stoichiometries and building blocks. Different thiophosphate microchemistries and single lithium counter ions are considered as building blocks. Only the dominant building blocks (e.g. PS_4^{3-} and $\text{P}_2\text{S}_7^{4-}$) are taken into consideration and utilized in a ratio that represents correctly the desired stoichiometry. For the Li_3PS_4 amorphous domain, hence, solely PS_4^{3-} tetrahedrons are used. The random sampling approach is conducted in the following way: First, the thiophosphate building blocks are rotated by a random angle and placed randomly on a predefined grid. Roughly 50 percent of the grid positions hereby remain empty. Thereupon, lithium ions are added into the structure utilizing a Voronoi Tessellation of the sulfur anion grid. The positions of P^{5+} ions are blocked to avoid their population. Voronoi Vertices are clustered with the aim to reach a number of clusters that correspond to the number of lithium ions necessary for charge neutrality.

A separate sampling of lithium ions and thiophosphate compounds has been shown to be beneficial to avoid large forces, as their requirements with respect to volume are substantially different.[50] The approach is designed in a way to yield a density of $\rho = 1.3 \text{ g cm}^{-1}$ at that point. This value is a trade-off between low densities, which ensure large P-P distances and hence prevent collision of thiophosphate compounds, and a sufficiently high density, which makes intermolecular interactions between separate thiophosphate units describable, as P-S distances lie in the cutoff (6 \AA) of the SOAP descriptor.[50]

The hereby obtained cell is then compressed to yield experimental densities in the range of 1.68 to 1.88 g cm^{-1} . [52] This is accomplished by iterative rescaling of the cell by a factor of 0.99 in all three directions in alternation with brief geometry optimizations (convergence criterion: $f_{max} = 3 \text{ eV/\AA}$) utilizing the GAP FF. The sampling approach is summarized visually in Figure 2.



Scheme 2: Graphical representation of the sampling approach, involving random sampling of thio-phosphate compounds on a predefined grid, addition of lithium ions via a Voronoi Tessellation of the anion grid, and iterative compressing to the desired density. Lithium is displayed in blue, phosphorous in violet, and sulfur in yellow

Training approach

As the explained training approach already utilizes the machine learning FF, it is reasonable to incorporate the sampling process into the training approach for the amorphous structure class. Hence, similar to the one executed for crystal structures (Figure 4), an iterative procedure is executed: training data for 10 sampled glass structures is generated via DFT and added to the training set of the GAP, which is subsequently retrained. Then, a new amorphous data set is generated with the current GAP FF. The iterative training cycle and the RMSEs of this iterative procedure are displayed in Figure 5 (Iterations 0-2).

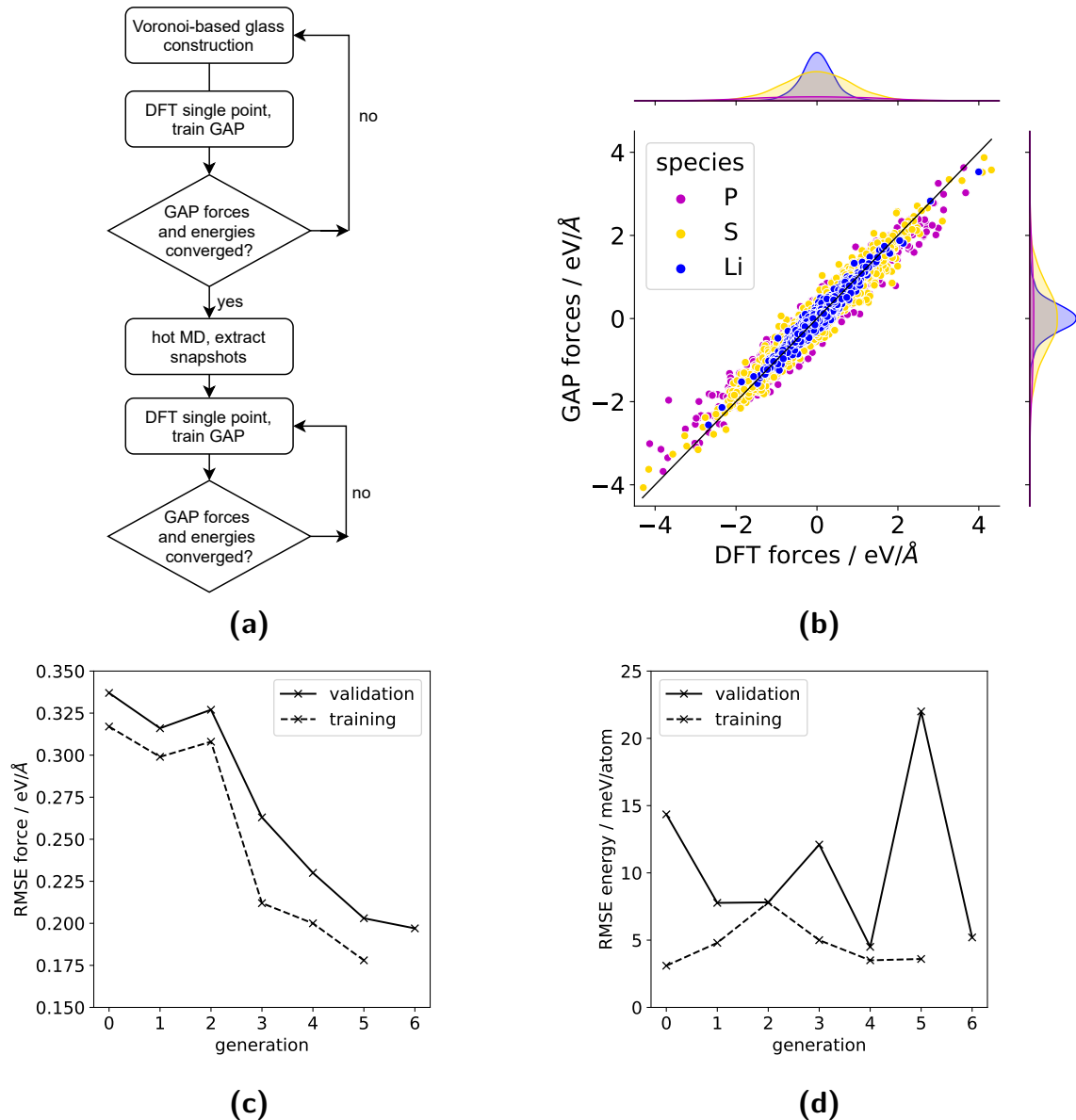


Figure 5: a) Workflow for the iterative training of amorphous LPS structures. b) Force correlation plot for the validation set of the last generation. c) Development of force error and d) energy error for training and validation set. Generation 0-2 corresponds to the sampling-based, generation 3-6 to the molecular dynamics-based training.

Convergence is reached at RMSEs of $0.3 \text{ eV}/\text{\AA}$ and $7.5 \text{ meV}/\text{atom}$ for forces and energies. The energy and force RMSEs obtained for the sampled amorphous structures are significantly higher than the values obtained for the equilibrated ones. This may be explained by the high (local) anisotropy of the training configurations: lithium ions are not evenly distributed and coordinated by a sphere of sulfur atoms, but often occur in clusters. The higher anisotropy is expected to increase the locality error induced by the finite cutoff of the SOAP descriptor.[51] To consequently obtain a glassy structure that represents the physical system, short molecular dynamics runs of the glasses at a temperature of 600 K are conducted and the iterative training

proceeded on these geometries, similarly to the training of crystalline geometries. Force and energy convergence in the iterative training cycle is shown in Figure 5c and d (Iterations 3-6). A significant decrease in force and energy RMSEs is observed as converged RMSEs of 0.2 eV/Å and 5 eV/atom are predicted.

The peak in RMSE energy of the validation set in generation 5 can be explained by the different temperature chosen for the MD run in this generation, which was 1000 K instead of 600 K. An elevated temperature, upon which the GAP is not yet trained, leads to a systematic underestimation of the energy. This effect is to be expected also for MD production runs at different temperatures, however, it does not pose a problem as the relative energy correlation within the set of structures is still very good. When correcting the GAP predicted energy for the observed offset, one obtains an energy RMSE of 0.005 eV/atom.

5.4 Training of further microchemistry: $\text{P}_2\text{S}_6^{4-}$

The next step in the training procedure of the machine learning force field is the extension of the local P-S microchemistry describable by the model. In particular, the emphasis is set on the $\text{P}_2\text{S}_6^{4-}$ building block. It is the most important compound which has been found frequently especially in glassy materials and is not yet in the training set as PS_4^{3-} and $\text{P}_2\text{S}_7^{4-}$. Specifically, $\text{P}_2\text{S}_6^{4-}$ is found exclusively in $\text{Li}_4\text{P}_2\text{S}_6$, a crystalline material with a remarkably low lithium ion conductivity. In contrast to the low crystalline conductivity, $\text{P}_2\text{S}_6^{4-}$ building blocks contribute significantly to conductive amorphous materials of variable Li_2S content.[16] The training is started using the most well-defined structure, which is the $\text{Li}_4\text{P}_2\text{S}_6$ crystal. An MD-based sampling like already introduced in Section 5.2 is conducted (iteration 0).

To continue, amorphous structures containing the building block are generated by adapting the sampling approach from Section 5.3. Glasses are sampled in the Li_3PS_4 stoichiometry by using PS_4^{3-} and $\text{P}_2\text{S}_6^{4-}$ building blocks in a ratio of 1:1. To retain the stoichiometry of Li_3PS_4 , two additional isolated sulfur atoms are added for every $\text{P}_2\text{S}_6^{4-}$ unit and placed together with the other thiophosphate components before the Voronoi Tessellation step. The $\text{P}_2\text{S}_6^{4-}$ ion is extracted from the $\text{Li}_4\text{P}_2\text{S}_6$ crystal.

However, it is observed that the $\text{P}_2\text{S}_6^{4-}$ units do not stay intact during the optimization but tend to either form structures which resemble the $\text{P}_2\text{S}_7^{4-}$ building block or collapse the P-P bond to unphysical distances below 0.5 Å. This can be intuitively explained as the force field had not been trained on different direct P-P bonds before and can hence not predict the energy profile on the P-P coordinate correctly. To prevent this unphysical behavior, the P-P bond distance is systematically sampled by distorting the $\text{Li}_4\text{P}_2\text{S}_6$ crystal and training the GAP on these geometries (training step 1). It is indeed found that the untrained GAP minimizes P-P distances. The minimized P-P distance is in contrast to the expected coulombic behavior in

DFT. When retraining on P-P DFT data, however, the GAP succeeds at predicting the correct energy profile. The distorted structures and the corresponding energy profiles of crystal, untrained and trained GAP are provided in Figure 6.

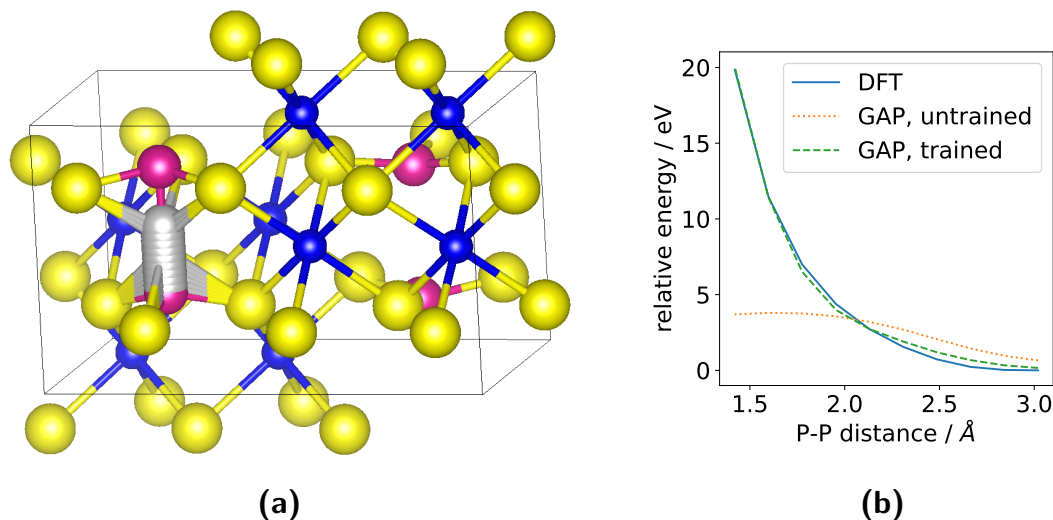


Figure 6: Systematic sampling of P-P distances in the $\text{Li}_4\text{P}_2\text{S}_6$ crystal. a) Geometries used for the sampling approach: The initial structure is distorted by displacing one phosphorous atom (i.e. shortening the P-P bond length). Lithium is displayed in blue, phosphorous in purple, sulfur in yellow, and the phosphorous atoms in the distorted structures in light grey. b) Obtained energy profile from DFT, untrained, and trained GAP as a function of P-P distance.

Subsequently, small glass cells solely containing $\text{P}_2\text{S}_6^{4-}$ units are built and relaxed using DFT. The $\text{P}_2\text{S}_6^{4-}$ microstructures obtained by DFT significantly differ from those found in $\text{Li}_4\text{P}_2\text{S}_6$, as the P-P distances collapse from 3.2 Å to 2.1 Å (Appendix, Figure 24a). The GAP is then trained on these geometries (training step 2) and related MD snapshots (training step 3). After these three steps, the iterative compressing of the amorphous structures is successful and two further training steps are executed with the obtained sampled glasses (training steps 4 and 5). A force correlation plot of the validation set from the last training iteration is shown in the Appendix, Figure 24b. The final RMSE values of forces and energies are 0.343 eV/Å and 4.5 meV/atom, which makes them comparable to the errors in the glass structures before MD equilibration (Figure 5c and d, iterations 0-2). RMSEs for training and validation of every training step are provided in the Appendix (Figure 23).

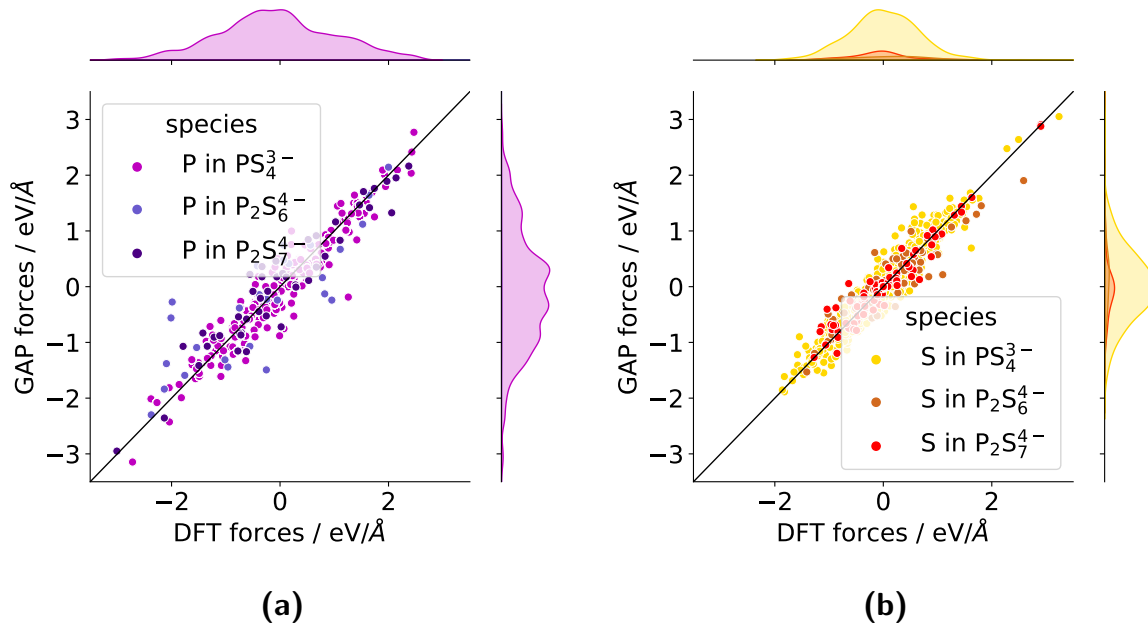


Figure 7: Coordination-resolved force correlation plot for P (a), and S (b) atoms in MD snapshots of $\text{Li}_7\text{P}_3\text{S}_{11}$ glasses.

A comparison of force RMSEs of phosphorous and sulfur in different P_mS_n polyhedra (Figure 7 and Table 2) proves, that RMSEs in $\text{P}_2\text{S}_6^{4-}$ are elevated in comparison to those in PS_4^{3-} and $\text{P}_2\text{S}_7^{4-}$. This may be attributed to the different charge states of phosphorous and sulfur or to non-ideal hyperparameters for this polyhedron.

Table 2: Coordination-resolved force RMSEs of phosphorous and sulphur in MD snapshots of $\text{Li}_7\text{P}_3\text{S}_{11}$ glasses.

polyhedron	RMSE phosphorous / $\text{eV}/\text{\AA}$	RMSE sulfur / $\text{eV}/\text{\AA}$
PS_4^{3-}	0.36	0.24
$\text{P}_2\text{S}_6^{4-}$	0.67	0.31
$\text{P}_2\text{S}_7^{4-}$	0.38	0.18

5.5 Random structure search

The conducted GAP training iterations from the previous sections allow the description of the main structural motifs in the LPS system: crystal phases (including all phases of Li_3PS_4 , $\text{Li}_7\text{P}_3\text{S}_{11}$ and $\text{Li}_4\text{P}_2\text{S}_6$), and glassy structures with different microchemical building blocks. However, it is unclear whether the whole configurational space which might be populated in the materials was covered by these training approaches. Training approaches are often human-biased. Hence, it is envisaged in this section to further extend the configurational space describable by the GAP using an unbiased approach: Random structure search (RSS). The approach might furthermore suit another purpose: It is desirable that the obtained GAP can not only describe the main structural features, but also the transitions between them. Hence, it provides a description for the reactivity of the material which might be especially important for the description of interfacial structures where structural changes take place. Two different RSS approaches are tested and discussed, which both show to not be suited well for the desired application.

GAP-RSS

The first strategy tested follows the idea to add structures to the training set, which are optimized using the current GAP. This GAP-RSS strategy has proven successful in the literature e.g. for elemental phosphorous.[53] For this aim 10000 structures are generated and the 20 most dissimilar ones selected by using farthest point sampling of the global Kernel matrix obtained from the SOAP descriptor. The 20 structures are then relaxed with a stop criterion of $f_{\text{max}} = 0.1 \text{ eV } \text{\AA}^{-1}$. An iterative training of the force field is then executed. The convergence behavior of the force field is shown in Figure 8.

What can be noted directly when comparing the force and energy RMSEs with the ones from the previous sections is that these are notably higher, especially for energies. This becomes even more pronounced when considering that the DFT forces in the structures are generally small, which should yield a smaller total RMSE. The absolute errors tend to be larger for higher forces, which is visible in e.g. the slope smaller than 1 in Figure 4. Additionally, it is apparent that no convergence of the force field is achieved, as the error is increasing again in iteration three. More iterations could be performed, but there is no indication that this approach will yield any further improvement.

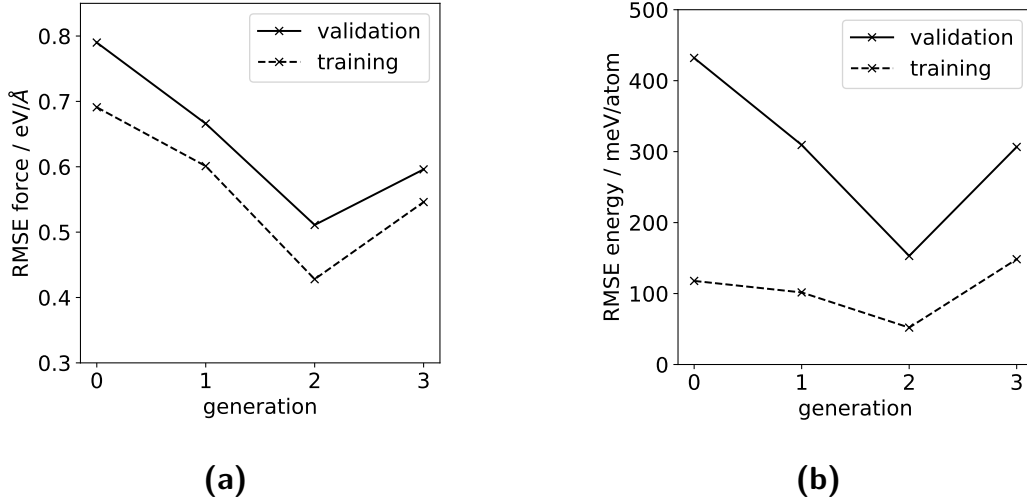


Figure 8: Convergence behavior of the force field during GAP-RSS for a) atomic forces and b) atomic energies.

AIRSS

Due to the problems encountered in the GAP-RSS strategy, a different approach is envisaged: training the force field via an *ab-initio* random structure search (AIRSS). In analogy to the first approach, the 30 candidates selected from the set of generated random structures are geometry-optimized, but in this case using forces from DFT, using a convergence criterion of $f_{max} = 0.01 \text{ eV } \text{\AA}^{-1}$.

When fitting the GAP on these structures, a large force RMSE of $0.70 \text{ eV } \text{\AA}^{-1}$ results, even though a significant improvement in comparison to the untrained GAP ($4.39 \text{ eV } \text{\AA}^{-1}$), yet is not satisfactory. Furthermore, the performance of the force field on crystal and glass structures is monitored and a disimprovement (force RMSEs for the glassy structures almost double) can be observed. This is highlighted in Figure 9. To improve the fit on the AIRSS structures, a force-dependent regularization approach is tested, where the regularization are tuned by using the following equation (proposed by Gabor Csanyi):

$$\sigma_F^i = \sigma_{min} + \frac{C}{A} \log_{10} \left(1 + A (\bar{F}^i + \frac{1}{n} \sum_i^n \bar{F}^i) \right) \quad (16)$$

\bar{F}^i denotes the magnitude of the force vector on atom i , n the number of atoms in a geometry and σ_{min} the minimum regularization onset. The parameters used are: $\sigma_{min} = 0.01 \text{ eV } \text{\AA}$, $C = 0.1$, and $A = 0.01$. GAP fits employing this regularization term significantly improve for the AIRSS set, yet perform equally worse for glass and crystal.

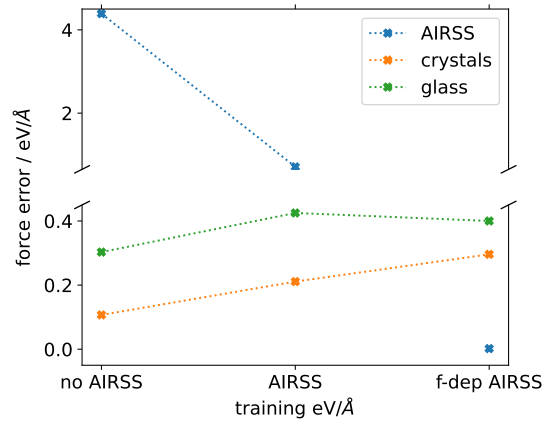


Figure 9: Force RMSEs of glass, crystal and AIRSS training set for different AIRSS conditions.

The problems encountered with the likewise GAP-RSS and AIRSS can be explained as follows: The number of minima on the potential energy surface scales exponentially with system size [54] and a local DFT optimization will converge automatically on the next minimum which is reached by simple force minimization. However, only a small subspace of these PES minima are physically relevant and will ever be reached by the system. Training the whole configurational space without any constraint will therefore necessarily lead to a disimprovement of the machine learning force field regarding the description of the desired subspace. Secondly, the iterative procedure will never converge due to the large number of local minima when training with configurations containing up to 20 atoms. Finally, it is rather pointless to neglect the physical knowledge on the material class, which comes down to chemical rules like phosphorous and lithium being coordinated by sulfur ions.

This intuitive explanation can be assessed quantitatively: For this purpose, the energy per atom of structures from different training sets is compared and the similarity of local environments is visualized using a 2D-kPCA plot (Figure 10). It is found that the energy of the GAP-RSS and AIRSS structures are not the issue: AIRSS structures are even lower in energy than the crystal representatives, which can be explained by the fact that the structures from the crystal were drawn from an MD at elevated temperature. This allows for the population of higher PES areas, while the AIRSS structures are geometrically relaxed. However, the similarity of local environments is very insightful: For glassy and crystalline structures, the local environments of the different atoms are clearly separated, in agreement with physical intuition. Yet, this separation is less evident for the GAP-RSS structures, and for AIRSS structures there is even an overlap of local environments found, which is not expected for physical representatives in the LPS structure class. The overlap being stronger for AIRSS also provides reasoning for the stronger disimprovement of glass and crystalline energies and forces. It can be concluded that a pure RSS approach is not suited to the aim described at the beginning of this section: an extension of the structural space sampled. Visually, this extension could be imagined as an

area surrounding the populated areas. When pursuing to further extend the configurational space further constraints would have to be imposed on the structures added to the training set. This could be achieved e.g. by predefining the P-S conductivity, which has however already been performed in the glass sampling process.

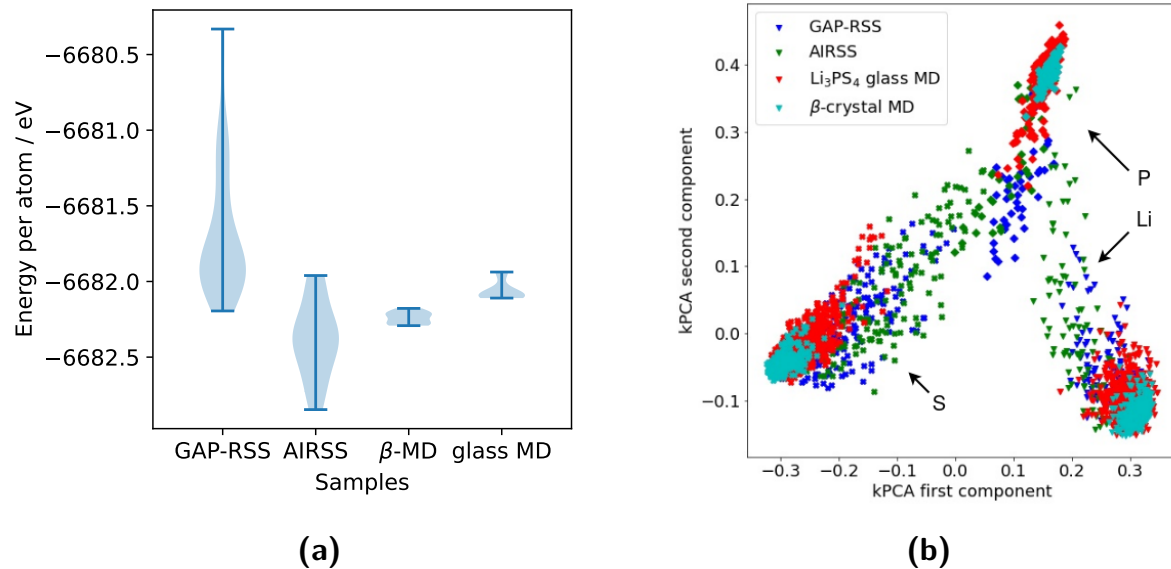


Figure 10: a) Violin plot comparing the energy distribution of RSS structures (GAP-RSS and AIRSS) to structures already in the training set (MD snapshots at 600 K from the β -crystal and the Li_3PS_4 amorphous structure). b) kPCA decomposition of local SOAP descriptors, comparing the same structures as in a). Lithium is indicated by triangles, sulfur by crosses and phosphorous by rhombs.

5.6 Thoughts on training of extended systems

It might be necessary to further retrain the ML potential when studying interfacial structures. Methods for this problem are not implemented in this thesis, but a brief overview of possible strategies is provided in the following section. Training the FF on extended systems like interface structures is a non-straightforward task, as those may consist of several thousand atoms. This is out of scope for DFT calculations. A workaround might be to target only the poorly described environments in the structure (in the following called target regions) and constrain DFT calculations to those. This approach would require 1. a metric to identify those regions and 2. a method that allows executing DFT calculations solely for them.

A metric for the identification of target regions can be provided by the local SOAP descriptor. The dissimilarity δ_{ξ_i} of a specific neighborhood from the training set can be defined by the minimum of the dissimilarity matrix $D_{\xi\xi'}$ (see Equation 14) in the respective row:

$$\delta_{\xi_i} = \max([D_{\xi\xi'}]_i) \quad (17)$$

Ideally, a dissimilarity threshold can then be defined, which would classify a region as target region when exceeded. First tests were executed using this approach, which showed that there is no direct correlation of force error and dissimilarity from the training set. This does not necessarily imply that a systematic selection of target regions does not provide an increased convergence in comparison to a random selection. Furthermore, a proper choice for the extension of the target region needs to be defined.

For the second task, two methods can be considered. First, a QM/MM scheme would allow for a precise description of the target region but limits the computational cost due to the coarse-grained description of the remaining structure.[55] However, a QM/MM scheme is not straightforward to implement for the LPS structure class, as electrostatic effects in the boundary region need to be addressed.[56] A different approach using state-of-the-art ML algorithms could aim at generating a small periodic cell that is representative for the target region, employing generative adversarial networks.[57]

6 Results from system characterization using the ML interatomic potential

The ML interatomic potential from the previous section is applied in the following to crystal, glassy, and interfacial structures. Central to this inquiry is the ionic conductivity σ^* . This property, arising from self-diffusivity of anionic and cationic species, can be obtained from the Nernst-Einstein relation:

$$\sigma^* = \frac{1}{3Vk_B T} \sum_{\alpha}^{n_{\alpha}} q_{\alpha}^2 N_{\alpha} D_{\alpha}^*. \quad (18)$$

V denotes the cell volume, k_B the Boltzmann constant, and T the temperature. The sum goes over all species α , with q_{α} , N_{α} and D_{α}^* denoting their respective charges, absolute number and (tracer) diffusion coefficients. Tracer diffusion coefficients D_{α}^* are derived by dividing the MSD (mean square displacement):

$$MSD(\tau) = \langle |r_i(\tau) - r_i(0)|^2 \rangle \quad (19)$$

by the total measuring time Δt and normalizing by the three spacial coordinates using the factor $\frac{1}{3}$: [58]

$$D_{\alpha}^* = \frac{1}{3} \frac{MSD(\tau)}{2\Delta t}. \quad (20)$$

$r_i(\tau)$ denotes the position of atom i at a specific lag time τ . The MSD can hence be directly obtained from MD runs and used to calculate the depending properties D_{α}^* and σ^* .

When performing a conductivity analysis for different temperatures, the activation barrier for ion diffusion E_A can be determined by plotting $\ln(\sigma T)$ as a function of inverse temperature (Arrhenius plot) and extracting the obtained slope of a linear fit. A denotes the pre-exponential factor.

$$\ln(\sigma T) = \frac{-E_A}{k_B T} + \ln(A) \quad (21)$$

6.1 Crystal

First, an ion conductivity analysis is conducted for crystalline phases Li_3PS_4 and $\text{Li}_7\text{P}_3\text{S}_{11}$. For Li_3PS_4 , α -, β -, and γ -crystals are studied.

A suitable temperature range for the simulations has to be chosen. First, the temperature should be high enough to yield sufficient ion diffusion and hence a good statistical ensemble in reasonable simulation times. Second, no structural change in the thiophosphate matrix (e.g. phase transition, melting) should occur in the chosen temperature range to make sure that the lithium ion conduction mechanism does not change for different temperatures and, consequently, the conductivities can be extrapolated to room temperature conditions. As a first guess, a temperature range of 500 to 1400 K is probed.

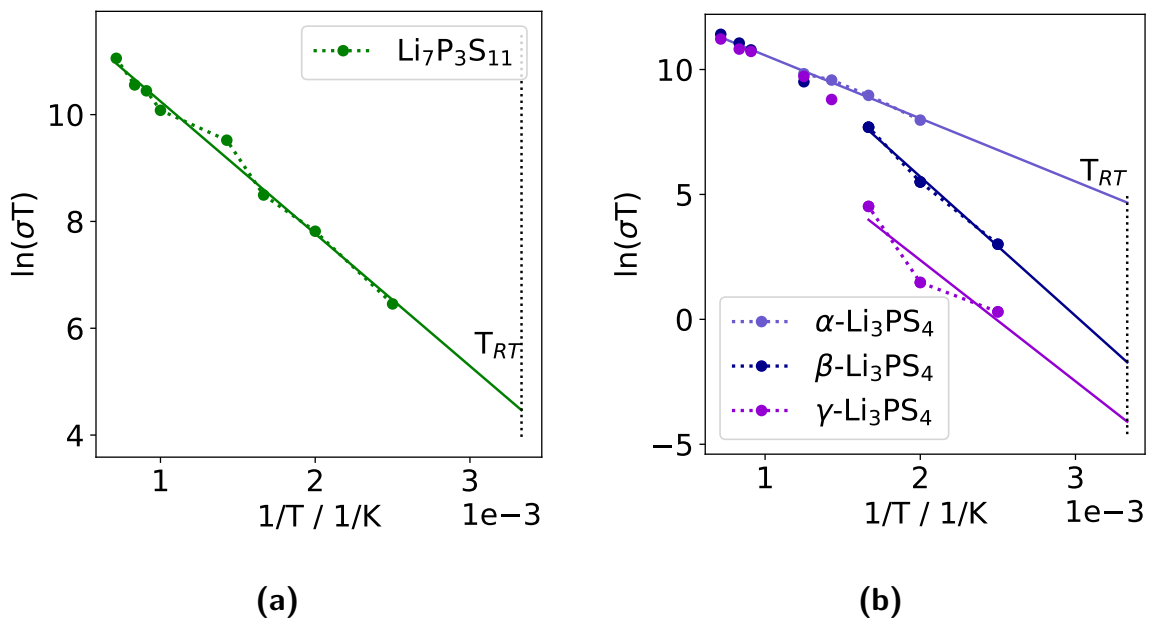


Figure 11: Computational Arrhenius plots for a) $\text{Li}_7\text{P}_3\text{S}_{11}$ and b) α , β and γ phase of Li_3PS_4 . Good correlations are found for $\text{Li}_7\text{P}_3\text{S}_{11}$. A phase transition to the α -phase explains the step in conductivity for β - and γ - Li_3PS_4 between 600 and 700 K.

Arrhenius plots for $\text{Li}_7\text{P}_3\text{S}_{11}$ and all phases of Li_3PS_4 are shown in Figure 11a and b. The activation energy E_A is extracted from the slope of linear regression, the room temperature conductivity σ_{RT} from an extrapolation of the linear fit. Obtained values are given in Table 3. For the case of $\text{Li}_7\text{P}_3\text{S}_{11}$, a linear behavior is found for the whole temperature range and an analysis of the trajectories reveals no structural change in the thiophosphate matrix. The extracted activation energy 0.21 ± 0.01 eV is in excellent agreement with AIMD calculations, [23] however experimentally reported activation energies span a broad range of 0.1 - 0.3 eV. [12, 13, 23] The obtained conductivity $2.9 \pm 1.1 \times 10^{-2} \text{ S cm}^{-1}$ can be considered an underestimation of the values from literature. Similar values have been reported in prior literature,

but also conductivities reaching $1.9 \times 10^{-2} \text{ S cm}^{-1}$, which are assumed to be reached by an increased crystallinity of the sample. An *ab-initio* study reports that the intrinsic conductivity of a perfect crystalline sample should be even higher ($5.7 \times 10^{-2} \text{ S cm}^{-1}$).[23] The Arrhenius curve of $\alpha\text{-Li}_3\text{PS}_4$ shows a linear behavior in the examined temperature range. An activation energy of $0.22 \pm 0.02 \text{ eV}$ and a σ_{RT} of $3.6 \pm 2.9 \times 10^{-3} \text{ S cm}^{-1}$ are obtained. This barrier is in good agreement with values obtained from AIMD calculations, which, however, report a σ_{RT} of $8.0 \times 10^{-2} \text{ S cm}^{-1}$. The Arrhenius curves of $\beta\text{-}$ and $\gamma\text{-Li}_3\text{PS}_4$ exhibit a tilt at roughly 700 K. When analyzing the thiophosphate matrix at different simulation temperatures, it is found that this tilt is caused by a phase transition to the $\alpha\text{-Li}_3\text{PS}_4$ structure, which involves a rotation of 25 % of the PS_4^{3-} tetrahedra by 180° for both structures.

This phase transition can be probed quantitatively by studying the radial distribution functions of the sulfur sublattice as a function of simulation temperature (Figure 12). The $\beta\text{-}$ and $\gamma\text{-}$ phase share an HCP (hexagonal close-packed) sublattice, which is transformed to a BCC (body centered cubic) lattice in the $\alpha\text{-}$ phase.[9] For both sublattices the S-S RDF displays a distinct peak at 3.4 \AA , which can be attributed to the intramolecular S-S distance. A second distinct peak at 4.3 \AA is observed in the HCP sublattice, which is lacking in the BCC structure. Both $\beta\text{-}$ and $\gamma\text{-}$ phase show the characteristic double-peak in the low-temperature RDF, while the second peak disappears for temperatures above 700 K.

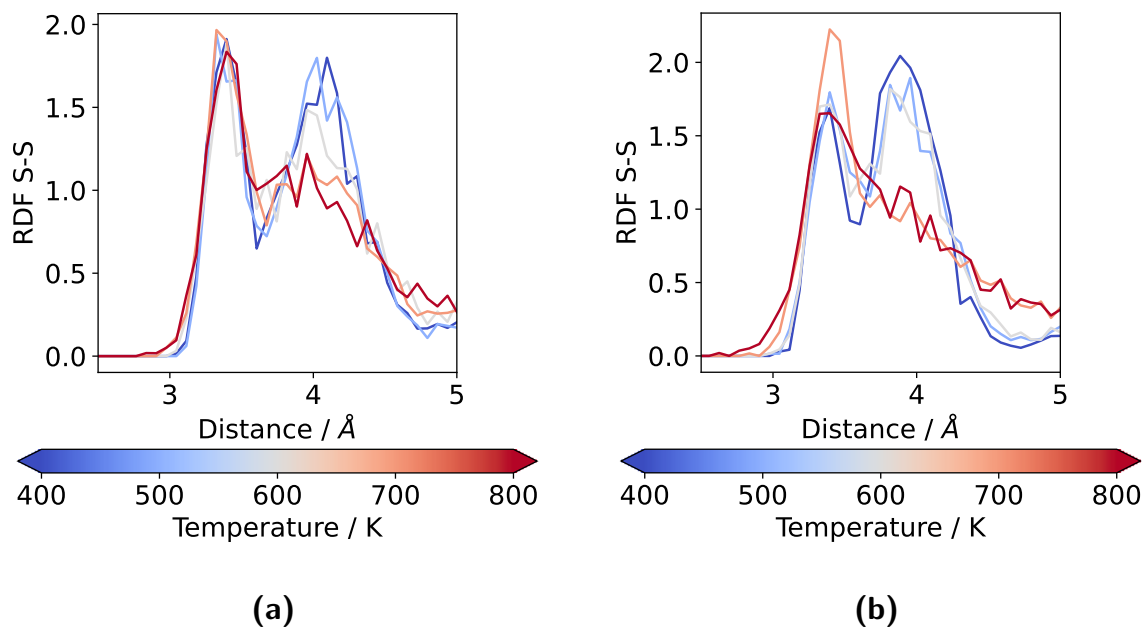


Figure 12: S-S RDFs for MD snapshots of a) $\beta\text{-Li}_3\text{PS}_4$ and b) $\gamma\text{-Li}_3\text{PS}_4$ at different temperatures. The disappearing of the peak at 4.3 \AA , occurring for both structures at 700 K, proves the phase transition to the $\alpha\text{-}$ phase.

Moreover, the same phase transition is observed in likewise experimental work and *ab-initio* simulations and the transition temperature between 600 and 700 K observed here matches the

experimentally reported temperature (746 K).[9, 18] However, an intermittent transition to the β -phase is predicted for γ -Li₃PS₄ at approximately 600 K by experimental studies,[18] yet does not occur in our findings. The conductivities of β - and γ -Li₃PS₄ above 700 K approximately match those of α -Li₃PS₄. Arrhenius plots of the two phases are hence only calculated with the data points between 400 and 600 K, obtained activation energies are given in Table 3. Those values are less interpretable than the ones obtained for Li₇P₃S₁₁ and α -Li₃PS₄, as a good statistic is hampered by these rather small temperatures for molecular dynamics in addition to generally small ion conductivities. The Einstein formulation (Equation 19) is only valid in the long time limit, which is achieved when the MSD displays a near linear behavior.[59] This is clearly not the case for the MD trajectories of γ -Li₃PS₄ (see Figure 25 in the Appendix). However, it can be said that the room temperature ion conductivity of the β -phase is significantly smaller than the one measured for the α -phase, and the one measured for γ smaller than the one obtained for β ($\sigma_{RT,\alpha} > \sigma_{RT,\beta} > \sigma_{RT,\gamma}$), both trends being in agreement with literature observations.[9, 18]

Table 3: Summarized conductivities from MD calculations performed in this study of the ternary LPS system in comparison to literature values. The abbreviations *aimd*, *ff* and *exp* denote that literature values are obtained from *ab-initio* molecular dynamics, molecular dynamics with classical force fields and experiment, respectively.

phase	σ_{RT} / S/cm	σ_{RT} , lit. / S/cm	E_A / eV	E_A , lit. / eV
Li ₇ P ₃ S ₁₁	$2.9 \pm 1.1 \times 10^{-3}$	5.6×10^{-2} , <i>aimd</i> [23]	0.21 ± 0.01	0.19 , <i>aimd</i> [23]
		1.2×10^{-2} , <i>exp</i> [23]		0.21 , <i>exp</i> [23]
		1.7×10^{-2} , <i>exp</i> [22]		0.17 , <i>exp</i> [22]
α -Li ₃ PS ₄	$3.6 \pm 2.9 \times 10^{-3}$	0.8×10^{-2} , <i>aimd</i> [9]	0.22 ± 0.02	0.18 , <i>aimd</i> [9]
β -Li ₃ PS ₄	$6.0 \pm 0.1 \times 10^{-5}$	8.9×10^{-7} , <i>exp</i> [18]	0.48 ± 0.04	0.46 , <i>exp</i> [6]
		10^{-1} , <i>aimd</i> [7]		0.16 , <i>exp</i> [18]
				0.08 , <i>aimd</i> [7]
				0.40 , <i>aimd</i> [60]
γ -Li ₃ PS ₄	$5.5 \pm 0.4 \times 10^{-7}$	3.0×10^{-7} , <i>exp</i> [18][6]	0.42 ± 0.16	0.49 , <i>exp</i> [6] 0.22 , <i>exp</i> [18]

6.2 Glass

The force field designed in Section 5 is the first machine learning force field enabling the investigation of amorphous materials in the structure class in their complexity (considering different stoichiometries and microchemistries) and likewise sufficient ensembles (regarding time ensembles in the form of sufficiently long MD runs and structural ensembles, considering the size of the cells and the number of studied structures in total). The following analysis aims to answer a set of questions: 1. Are the glassy structures obtained from the sampling approach in Section 5.3 reasonable concerning isotropicity and local structure, and do they represent the physical system? 2. In which ratios do thiophosphate building blocks occur and are these ratios temperature-dependent as predicted in literature? 3. What is the influence of the observed building block ratios on the lithium ion conductivity of the material?

To have a sufficient ensemble average, 20 structures are generated for each calculation employing the same conditions (e.g. at a specific temperature or stoichiometry). Structures are built exclusively using a target density of 1.8 g cm^{-3} , as preceding tests have shown that neither structure nor conductivity change significantly in the prescanned density range ($1.7 - 1.9 \text{ g cm}^{-3}$). This is in line with literature findings.[61] The tests are summarized in the Appendix (Figure 27). A density of 1.8 g cm^{-3} is selected as it has been predicted by AIMD studies.[8] Experimental studies also report similar values.[16] Three different stoichiometries are considered in the analysis, covering the range from mostly tetrahedral (Li_3PS_4) to mixed ($\text{Li}_7\text{P}_3\text{S}_{11}$) to mostly bridged tetrahedral ($\text{Li}_4\text{P}_2\text{S}_7$) thiophosphate moieties. Although it would in principle be possible to directly sample the reported polyhedron ratios from literature, PS_4^{3-} and $\text{P}_2\text{S}_7^{4-}$ building blocks are sampled exclusively in ratios that fulfill the desired stoichiometries (see Table 4).

To find a suitable temperature range for the conductivity analysis of amorphous structures, the mean square displacements of the non-mobile species sulfur and phosphorous are monitored. In the desired temperature range the material is expected to exhibit no S and P diffusion. Hence, convergence of the mean square displacement after a certain equilibration period is desired. It is found that - independent of stoichiometry - a relevant diffusion of both sulfur and phosphorous occurs above a temperature of 700 K. Mean square displacements are shown in the Appendix (Figure 28). Hence, temperatures between 400 and 700 K are selected for the conductivity analysis.

Table 4: Glass stoichiometries used for the analysis, their corresponding Li_2S content, and ideal building block ratios.

Stoichiometry	Mol % Li_2S	(ideal) ratio $\text{PS}_4^{3-}/\text{P}_2\text{S}_7^{4-}$
Li_3PS_4	75	1:0
$\text{Li}_7\text{P}_3\text{S}_{11}$	71.5	1:1
$\text{Li}_4\text{P}_2\text{S}_7$	70	0:1

6.2.1 Chemical reasonability and microchemistry

First, the structure is analyzed on its chemical reasonability based on several complementary criteria. The first one is the plausibility of the obtained local environments, regarding bonding distances and conductivity patterns, and further the amorphous nature. A good measure therefore are radial distribution functions: The element-resolved radial distribution functions for glassy Li_3PS_4 along with the crystalline counterparts (α -, β -, and γ - Li_3PS_4) are displayed in Figure 13.

It is apparent that the P-S and S-Li radial distribution functions of glass and crystal are identical. Differences occur for S-S, where a double peak at around 4 Å is observed for the β - and γ -crystal, but neither for the α -phase nor for the amorphous structures. Kim *et al.* have used this peak in literature to discriminate between hexagonal and cubic S-sublattices in the structure.[17] The P-P RDF displays differences as well: In the amorphous material two peaks are observed which are not found in the crystals, located at 2 - 2.5 Å and 3 - 3.5 Å. These peaks can be attributed to the occurrence of $\text{P}_2\text{S}_6^{4-}$ and $\text{P}_2\text{S}_7^{4-}$ moieties.

Another distinction can be made for the peaks at $r_{\text{P-P}} \leq 4.5$ Å: Two distinct peaks occur in all crystal phases, while one broad peak is visible for the glass. This observation is a validation for the non-periodicity of the P-lattice in the amorphous material.

A second measure for the amorphous nature of the glasses is isotropicity with respect to the ion diffusivity in all dimensions. This is tested using an ensemble of 20 MD runs of Li_3PS_4 glass at 500 K. It is found that the standard deviation of the mean square displacement in x, y, and z direction vary by 9 % in one MD run, but by only 1 % when averaging over the 20 structures in the ensemble. Hence, the structures are sufficiently isotropic with respect to diffusivity.

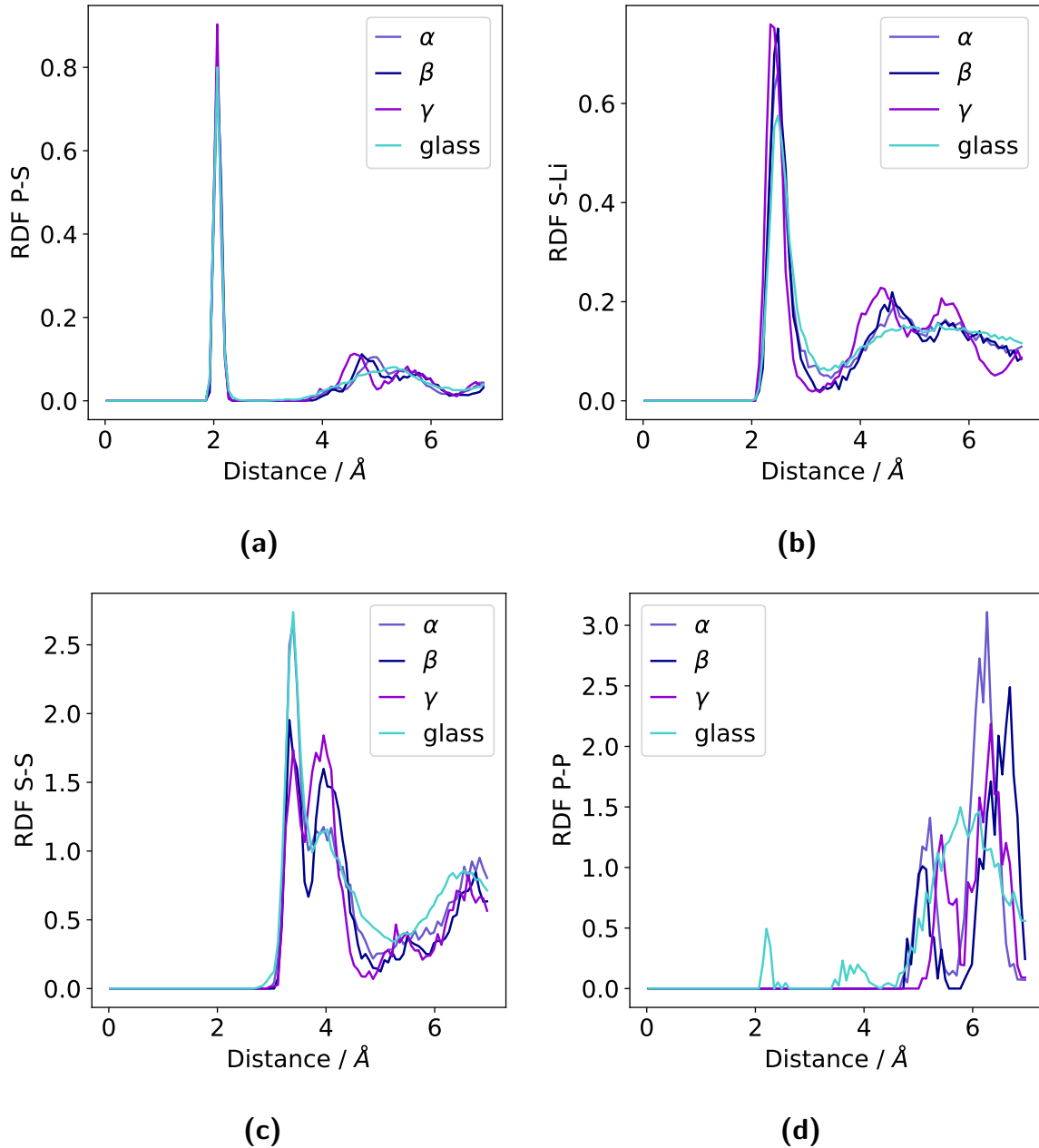


Figure 13: Radial distribution functions for a) P-S, b) S-Li, c) S-S and d) P-P, collected from molecular dynamics runs of α , β , and γ -crystals at 500K, using an averaged ensemble of 20 different Li_3PS_4 glasses with $\rho = 1.8 \text{ g cm}^{-3}$.

After a general look at structural plausibility, a more detailed analysis is performed focusing on the different thiophosphate building blocks. As a metric to determine the ratios of different polyhedra in the structure, the P-P distance is used. Distances below 2.5 \AA are attributed to $\text{P}_2\text{S}_6^{4-}$ moieties, distances between 2.5 and 4.5 \AA to $\text{P}_2\text{S}_7^{4-}$, and the remaining phosphorous atoms are assigned to PS_4^{3-} . First, it is studied whether the polyhedron ratios change over time during single MD runs. It is found that compound formation takes place at the beginning of the MD run and the obtained ratios do not change significantly throughout the run.

Especially the formation of $P_2S_6^{4-}$ polyhedra is predicted to be irreversible by the FF. Secondly, it is interesting to examine whether the temperature dependence of building block occurrence predicted in experiments (the $P_2S_6^{4-}$ content is predicted to strongly increase for Li_2S contents below 0.75, attributable mainly to the formation of crystalline $Li_4P_2S_6$) can be reproduced. Violin plots for all three stoichiometries, showing the building block distributions at different temperatures using the 20 structure ensembles, are displayed in Figure 14. The temperature range motivated in Section 6.2 is used and a high-temperature reference at 1000 K is added.

For the case of Li_3PS_4 , PS_4^{3-} is the predominating species over the whole temperature range. $P_2S_6^{4-}$ occurs only in small concentrations < 10 at.%. and shows no strong temperature dependence, whereas up to 25 at.% of $P_2S_7^{4-}$ occur at the lower temperature but diminish between 600 and 700 K.

For likewise $Li_7P_3S_{11}$ and $Li_4P_2S_7$, the $P_2S_6^{4-}$ content increases between 400 and 700 K. The increase is not pronounced in comparison to the width of the distribution in the ensemble.

When comparing the building block ratios to those reported in experiments, the values found for Li_3PS_4 fit the experimental data well.[16] Overestimated $P_2S_6^{4-}$ contents are found in $Li_7P_3S_{11}$ and $Li_4P_2S_7$, attributable to an overestimated tendency of the $P_2S_7^{4-}$ building block to form direct P-P bonds.

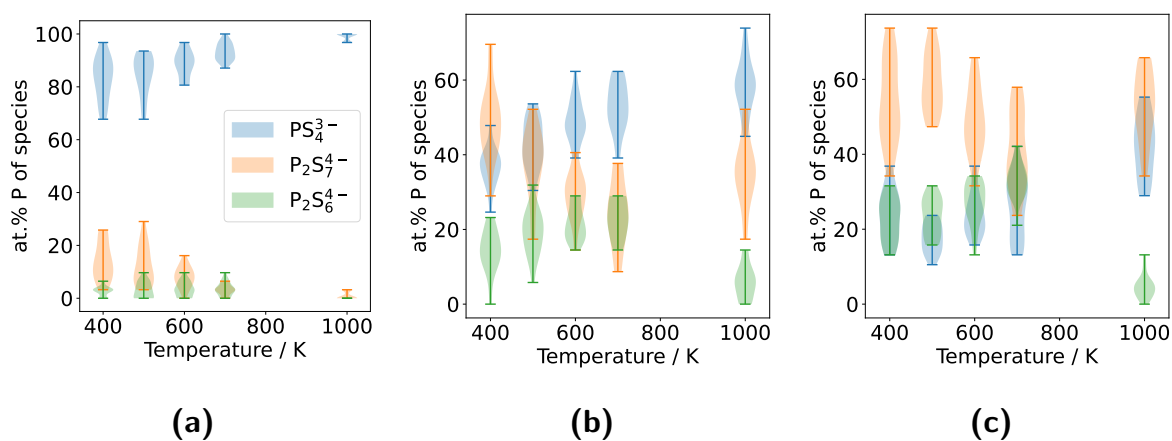


Figure 14: Average building block compositions for different MD temperatures, displayed for a) Li_3PS_4 , b) $Li_7P_3S_{11}$, and c) $Li_4P_2S_7$.

6.2.2 Conductivity

Before the additional examination of the obtained ratios, it should be addressed if the lithium ion conductivity depends on those. Figure 15 reports all the conductivities obtained at different temperatures as a function of their respective $P_2S_n^{4-}$ content ($n = 6,7$). The temperature

dependence of the conductivity is much stronger than the dependence on building block ratios. However, it is analyzed employing Pearson correlation coefficients whether a certain correlation between conductivity and building block ratios exists. The coefficient is a measure for linear correlation of two variables X and Y , defined by dividing their covariance by the product of their standard deviations:

$$\rho = \frac{Cov(X, Y)}{\sigma_X \sigma_Y}. \quad (22)$$

Negative correlation coefficients in the range $[-0.4, -0.2]$ are found almost consistently for the different stoichiometries and temperatures. The results are summarized in the Appendix (Table 7). However, the magnitude of the correlation coefficients is not large enough to make this weak trend of decreased conductivity with increased $P_2S_n^{4-}$ content significant. An identical analysis is performed monitoring the $P_2S_6^{4-}$ and $P_2S_7^{4-}$ contents separately, which yields even less pronounced trends.

Literature data on the effect of polyhedra ratios on conductivities is quite controversial. On one hand studies report on a strong conductivity suppression by $P_2S_6^{4-}$, [12, 62] which most likely arises from precipitation of the non-conducting $Li_2P_2S_6$ phase. *Ab-initio* calculations report that on the other hand $P_2S_7^{4-}$ should suppress ion conduction, as its coulombic interaction with the lithium ion is stronger than the one of the other thiophosphates. [25] One effect which has been unconsidered up to now is that the formation of $P_2S_n^{4-}$ in Li_3PS_4 either is driven by sulfur deficiency or will result in uncoordinated sulfur anions occurring in the structure. Those might hinder lithium ion diffusion by the formation of ionic Li-S bonds. This influence however cannot be studied with the available FF, as it cannot distinguish different charge states of sulfur. Ideas on how to tackle this problem are discussed in the Outlook (Section 7).

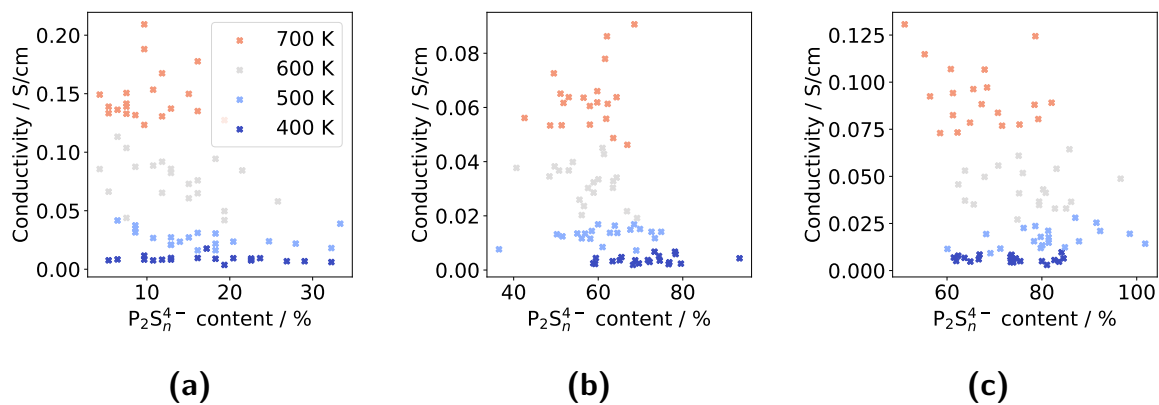


Figure 15: Conductivity as a function of $P_2S_n^{4-}$ ($n = 6, 7$) content in the glassy structure for a) Li_3PS_4 , b) $Li_7P_3S_{11}$, and c) $Li_4P_2S_7$. No correlation is observed for any combination of stoichiometry and temperature.

All structures of the calculated ensembles are used to perform an Arrhenius analysis, presented in Figure 16. The linear regression is performed including error weighting of the y values. A

linear behaviour is found in the investigated temperature range for all stoichiometries. The extracted activation energies (Table 5) are almost alike and closely below 0.3 eV. Experimental and theoretical results range from 0.25 to 0.38 eV.[8, 16, 17, 63]

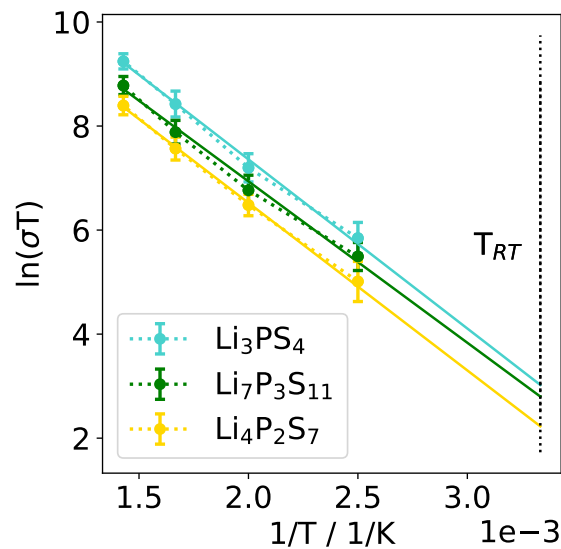


Figure 16: Arrhenius plot for the three glass stoichiometries, using an ensemble of 20 structures for each temperature and MD runs of 1.5 ns length. It is found that all glasses have alike activation barriers for diffusion.

The ion conductivity over the whole temperature range and further obtained RT ion conductivities increase alongside the Li_2S content of the glass material, yielding a doubling of conductivity from $\text{Li}_4\text{P}_2\text{S}_7$ to Li_3PS_4 . Differences can be attributed to a variation in the intrinsic conductivity, as activation barriers are comparable. Partly, they are attributable to the lithium mass percentage increase at equal densities. This larger concentration of charge carriers yields higher conductivities for similar diffusion coefficients (see Equation 18), accounting for an increase in conductivity of 30%. The conductivity increase with higher Li_2S contents, which is not attributable to the difference in mass percentage, might arise from the different contents of $\text{P}_2\text{S}_n^{4-}$, following the (weak) trend identified before. An intuitive explanation for this trend might be that the space demanding $\text{P}_2\text{S}_n^{4-}$ moieties allow for less lithium ion diffusion channels in the material than the smaller PS_4^{3-} units. For all glasses, an absolute ion conductivity at RT between 10^{-4} and $10^{-3} \text{ S cm}^{-1}$ is found.

A literature comparison with theoretical values yields a good agreement with predictions of a classical force fields [17] (σ_{RT} of $4.08 \times 10^{-4} \text{ S cm}^{-1}$) and a five times lower conductivity than reported from AIMD simulations, which however used smaller cells containing 130 atoms and very short production steps of 10 ps.[8] The trend of a slightly increasing conductivity

with increasing Li_2S content is also reported in the *ab-initio* study, yet is predicted to be less pronounced.[8] Experimental values range from 10^{-5} to 10^{-3} S/cm. [16, 20, 27]

Table 5: Summarized conductivities for the three glass stoichiometries examined in this study in comparison to literature values. The abbreviations *aimd*, *ff* and *exp* denote that literature values are obtained from *ab-initio* molecular dynamics, molecular dynamics with classical force fields and experiment, respectively,

Stoichiometry	σ_{RT} / S/cm	σ_{RT} , lit. / S/cm	E_A / eV	E_A , lit. / eV
Li_3PS_4	$6.9 \pm 0.9 \times 10^{-4}$	4.1×10^{-4} , <i>ff</i> [17]	0.280 ± 0.003	0.28 , <i>ff</i> [17]
		8.8×10^{-5} , <i>aimd</i> [8]		0.17 , <i>aimd</i> [8]
		2.8×10^{-4} , <i>exp</i> [16]		0.40 , <i>exp</i> [16]
		7.5×10^{-4} , <i>exp</i> [20]		
$\text{Li}_7\text{P}_3\text{S}_{11}$	$5.5 \pm 0.8 \times 10^{-4}$	8.2×10^{-5} , <i>aimd</i> [8]	0.267 ± 0.003	0.45 , <i>exp</i> [16]
		3.7×10^{-5} , <i>exp</i> [16]		
		1×10^{-4} , <i>exp</i> [27]		
$\text{Li}_4\text{P}_2\text{S}_7$	$3.1 \pm 0.2 \times 10^{-4}$	5.7×10^{-5} , <i>aimd</i> [8]	0.278 ± 0.002	0.44 , <i>exp</i> [16]
		3.8×10^{-5} , <i>exp</i> [16]		

6.3 Interface

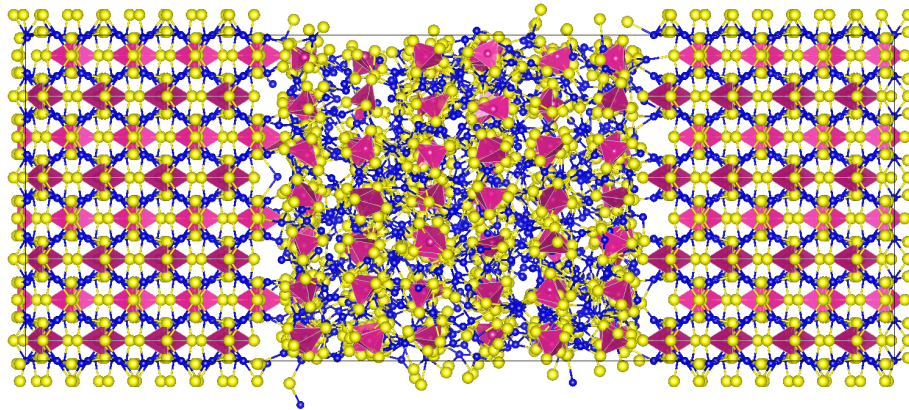
After an in-depth analysis of purely crystalline or amorphous materials, those are combined in this section to yield glass-crystal interfaces. It is aimed to study the resulting interfacial structures and the effect of the boundary region on lithium ion conduction. The combinatorial possibilities of interfaces are huge, as the study of several crystal phases and exposed surface indexes are possible. Results presented here focus on the β -phase of Li_3PS_4 and only investigate the low index surfaces (100), (010), (001), plus the $(\bar{1}10)$ surface as this has been found experimentally in glass-ceramics of Li_3PS_4 .^[15] This crystal phase is selected, as a significant increase in conductivity was found in literature when comparing the pure crystal to a glass-ceramics structure.^[6, 10] The assembly protocol presented in the following can however be extended to any desirable crystal and surface combination.

6.3.1 Building and sintering

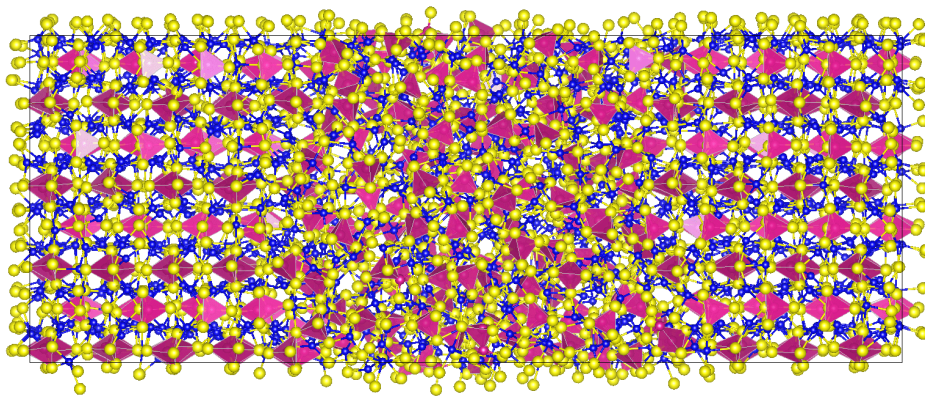
The construction of the interface model is inspired by previous work in the group.^[46] The interface model is built by first constructing a $4 \times 4 \times 4$ supercell of the β -crystal and doubling the size once more in the direction perpendicular to the exposed crystal surface. Then, the crystal is placed into a cell, where the cell vector in the interface direction is doubled in length. The crystal is moved to yield a void in the center of the cell, which is supposed to host the amorphous counterpart. The total structure consists of approximately 3000 atoms. A sampling and compression procedure alike to the one presented in Section 5.3 is conducted, with the difference that compression is performed only in the interface direction. To equilibrate the boundary region the next step is a simple sintering protocol. It consists of stepwise heating of the system to a temperature of 1000 K and a subsequent stepwise cooling using simulated annealing, which involves an increase of simulation time with decreasing temperature. The temperature profile of the protocol is shown in the Appendix (Figure 29). Exemplary structures before and after sintering are shown in Figure 17.

6.3.2 Characterization

In the following, the obtained interface models are characterized to answer the following questions: Is the interface structure fundamentally different from the one of glass and crystal, or can it rather be considered a mixture of both? Derived from that, is the current ML FF able to describe the interfacial region, or is a retraining procedure like proposed in Section



(a)



(b)

Figure 17: Interface model for β -Li₃PS₄ and the (110)-surface termination a) before equilibration and b) after equilibration. Lithium is displayed in blue, phosphorous in violet, and sulfur in yellow

5.6 necessary? Finally, it should be assessed if there is any trend regarding the occurrence of different P_mS_n building blocks in the interfacial region.

The first part of the characterization is the analysis of the formed boundary region between glassy and crystalline structures. A metric based on a Fourier transformation of the phosphorous grid is employed to analyze the degree of amorphization F across the interface coordinate z . A Fourier transform of Gaussian-smearred atomic coordinates, projected in 2D, is calculated and the sum over Fourier intensities normalized to its maximum value I_{max} defined as: [46]

$$F(z) = \frac{\sum_{xy} I_{2D-FFT}(z)}{\sum_{xy} I_{max}}. \quad (23)$$

Amorphization profiles are presented in Figure 18. For all structures, clear discrimination between crystal and glassy domains can be made and a continuous increase in amorphization can be seen in the interface regions. The width of these boundary regions can be determined by using the onset and offset of the amorphization increase. It is found that - independent of

the surface index - a narrow interfacial region of approximately 7 Å in width is formed.

The only report on an atomistically studied glass-crystalline interface of Li_3PS_4 by Kim *et al.* found a boundary region of approximately 15 - 20 Å width, obtained via analysis of the S-sublattice.[17] However, an analysis of their interface structure with our metric yields a width of only 10 Å, which is similar to the 7 Å found in this study.

Yet it remains to be assessed whether width and structure of the interfacial region depend on the employed sintering protocol. Tunable parameters are the maximal temperature or the sintering length. In this example, a temperature of 1000 K has been chosen to avoid melting of the crystal phase. A relatively short sintering time of 150 ps has been chosen due to computational limitations in our approach.

The identified boundary region is structurally analyzed in the following, using the already fa-

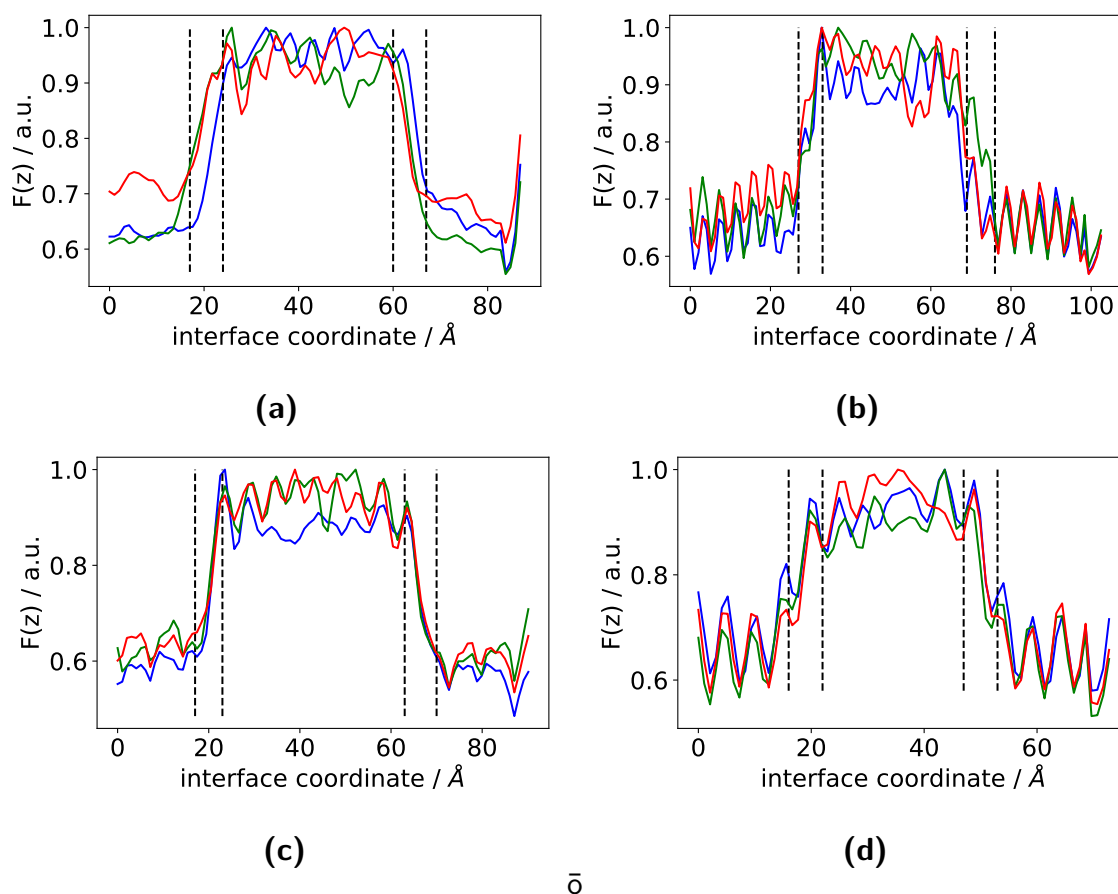


Figure 18: Degree of amorphization across the interface coordinate for a) (100), b) (010), c) (001) and d) ($\bar{1}10$) interfaces, probing an ensemble of three structures for every surface index (displayed in blue, green and red). For all surfaces, the boundary regions are marked with dotted lines. The width of the interfacial regions is approximately 7 Å, independent of surface termination.

miliar metrics of the SOAP descriptor and the RDF. Partial RDFs of the crystalline, interfacial, and glassy regions are presented in Figure 19. The P-P RDF of the interface displays the same two low-distance peaks (2 and 4 Å) as found in the glass. Those are attributable to $\text{P}_2\text{S}_6^{4-}$

and $\text{P}_2\text{S}_7^{4-}$, respectively. The two higher-distance peaks at 5.5 and 6.5 Å characteristic for the crystal are still visible in the interface, yet already broadened. A single broad peak is found in the glass. The S-S RDF of the interface exhibits the double peak found in the crystalline structure, yet, the second peak is less pronounced. The functional profile hence is a mixture of the one found in glass and crystal.

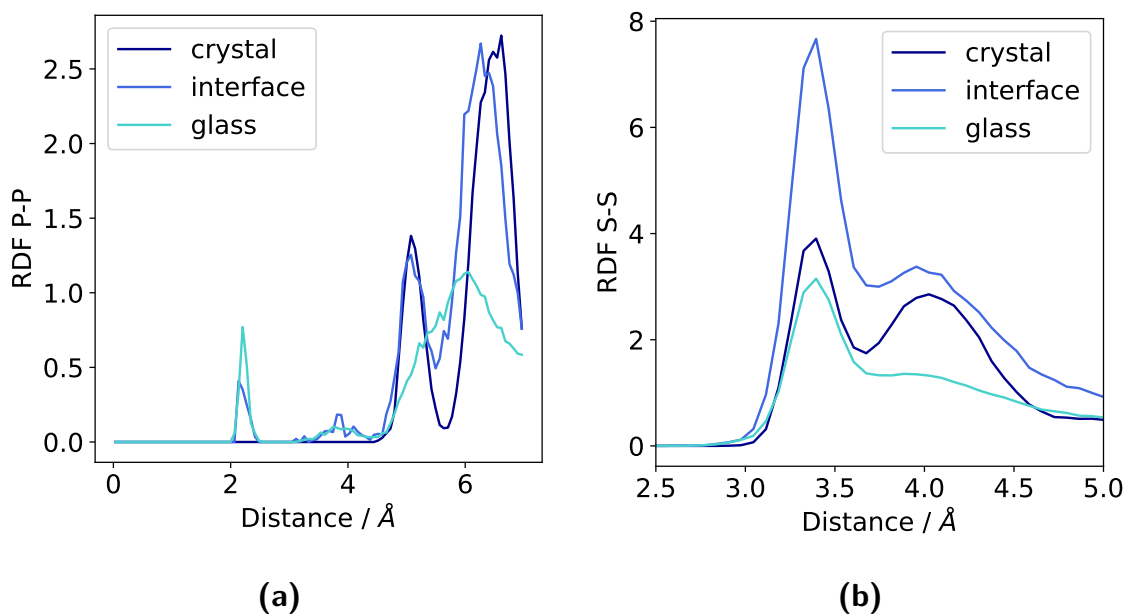


Figure 19: Region-resolved P-P (a) and S-S (b) radial distribution functions of the interface structure. The functions are averaged over interfaces of all four examined surface orientations, as they do not exhibit significant differences.

In addition to the RDF analysis, the interfacial structure is compared to glass and crystal using the local SOAP similarity metric. The analysis is conducted for phosphorous and sulfur, as lithium is the mobile species with a non-fixed chemical neighborhood. Similarity plots are shown in Figure 20. Structural similarity of the interface to glass and crystal is found, meaning that no completely new areas of the configurational space are occupied. The set of outliers in the plot for sulfur can be attributed to single sulfur ions which are not P-bound and hence found dominantly in the interface and the glass domain.

To sum up the findings of the structural analysis, no structural features unique to the interfacial region are found. Rather, the region can be described as a smooth transitioning from the crystalline to amorphous structure.

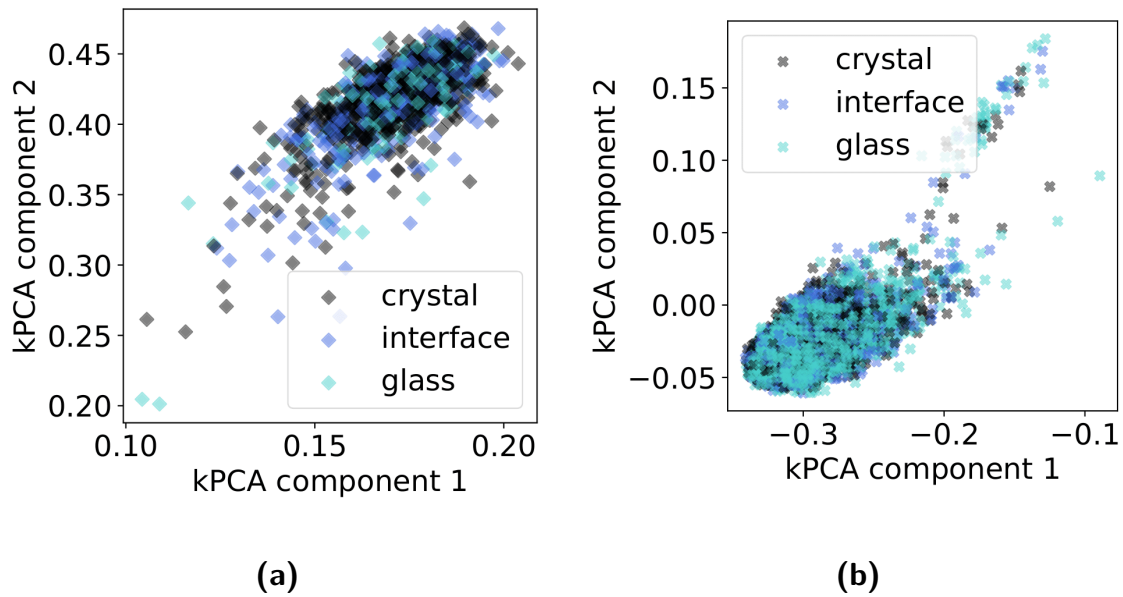


Figure 20: kPCA plots of SOAP dissimilarity for phosphorous (a) and sulfur (b), highlighting that there is no fundamental structural difference of the interface from the glass- and crystalline structures.

6.3.3 Conductivities

The lithium ion conductivity, averaged over all surface orientations, of the whole interface model is determined as $2.4 \pm 0.3 \cdot 10^{-3} \text{ S/cm}$, which corresponds approximately to the one of the Li_3PS_4 glass at the same temperature. Furthermore, the MSDs of lithium ions in different domains is calculated by assigning the ions to a fixed domain, using their average position over the course of the trajectory. Figure 21 depicts the results for all four surface terminations. No significant difference of the MSDs in the three domains is found, which is surprising, as the conductivity of the pure Li_3PS_4 crystal is approximately a factor of four lower than the one of the glass at 500 K. This preliminary result is somewhat in agreement with experimental literature, where the conductivity of glass-ceramics is closer to the one of the glassy than the crystalline domain. Yet, there is no physical explanation for this observation, as it is unclear how the lithium ion mobility in the crystal can be influenced by the neighboring amorphous domain. However, this result is only preliminary and further investigations should be carried out, e.g. by virtue of MD runs at different temperatures (the conductivity difference between glass and crystal should be more pronounced at lower temperatures due to the different activation barriers) or direction-resolved analysis of the MSD.

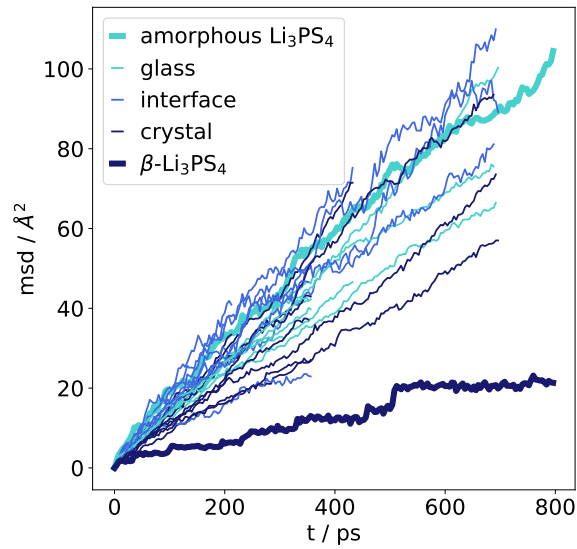


Figure 21: Lithium MSD for glass, crystal, and interfacial region in comparison to the MSDs of β - Li_3PS_4 and amorphous Li_3PS_4 . Trajectories from interfaces with all previously mentioned surface terminations are shown.

It should also be considered that this effect is caused to some extent by the fixed assignment of ions to one domain, which does not take an inter-domain migration into account. Hence, it should be envisaged to implement a more sophisticated dynamic assignment of ions to specific domains.

7 Conclusion and outlook

Conclusion In this thesis, a ML atomistic potential for the LPS material class has been developed, which is familiar to the predominant chemistry occurring in the structure class, covering different P_mS_n polyhedra and degrees of periodicity (crystal, glass). For all stoichiometries, a good correlation with PBE reference calculations was achieved. However, $P_2S_6^{4-}$ polyhedra are described with lower accuracy than PS_4^{3-} and $P_2S_7^{4-}$.

The potential was applied to a set of materials to probe lithium ion conduction. For the crystalline materials, excellent agreements of activation energies from AIMD and experimental studies was achieved. The phase transitions occurring in the Li_3PS_4 stoichiometries and the accompanied conductivity increases were reproduced. Amorphous materials of the $xLi_2S-(100-x)P_2S_5$ type with variable Li_2S contents were investigated ($x = 67, 70, 75$). Especially, a focus was set on the structural variability of the occurring polyhedra P_mS_n . No strong influence of the polyhedra ratios on lithium ion conduction was found. Nonetheless the conductivity has proven to increase along with the Li_2S content, which was partially attributed to the higher volume density of lithium ions. Furthermore, an influence caused by uncoordinated S^{2-} ions is suspected, but can not be accessed with the charge-free ML FF. Preliminary investigations on glass-ceramic interfaces were executed, using the β - Li_3PS_4 crystal as ceramic phase and probing low-index surfaces. The interfaces were assembled using a simple sintering protocol and the interfacial structure was investigated. This revealed that the boundary region contains characteristics of both glassy and crystalline phase, but does not feature any new chemistry. A domain-resolved lithium ion mobility analysis further suggested that lithium is equally mobile in all domains. This requires further investigation, but is an interesting finding which might explain increased lithium ion conductivities in glass-ceramic materials of β - Li_3PS_4 .

Outlook The machine learned FF could be used for more extensive studies, including in principle all structure classes. Open questions, such as the origin of the predicted low conductivity of Li_3PS_4 in comparison to *ab-initio* studies, remain. The predicted conductivity is much closer to prior experiment reports, but the physical reason for this observation remains unclear and e.g. a systematic study of the occupation of interstitial lithium sites could deliver an explanation.

Considering the interface model, a more systematic assessment of sintering protocols and their influence on the obtained interfacial region might be considered, alongside more sophisticated analysis methods for lithium ion diffusion.

From a methodological point of view, several improvements to the developed FF should be envisaged. First, an improved implementation of the SOAP descriptor, called *turbo*-SOAP, has recently been shown to improve both the accuracy and the efficiency of a GAP model.[64]

Besides saving computational resources, the factor 10 speedup could allow for an extension of simulation time and system size of the proposed interface models. Second, a profound limitation of the FF is its lack of charges. Those might be essential e.g. for the description of lithium ions with uncoordinated sulfur counter ions, as already suggested in Section 6.2. Furthermore, the behavior of the system under an applied potential cannot be studied. A promising approach to implement charges into the FF, which is currently developed in the group, is KernelQeQ.[65] In the previously mentioned electrostatic GAP model a electrostatic baseline model using fixed charges is used. Replacing this simple fixed charge model by KernelQeQ will yield extensive improvements of the electrostatic GAP model.

8 Appendix

8.1 FF Training

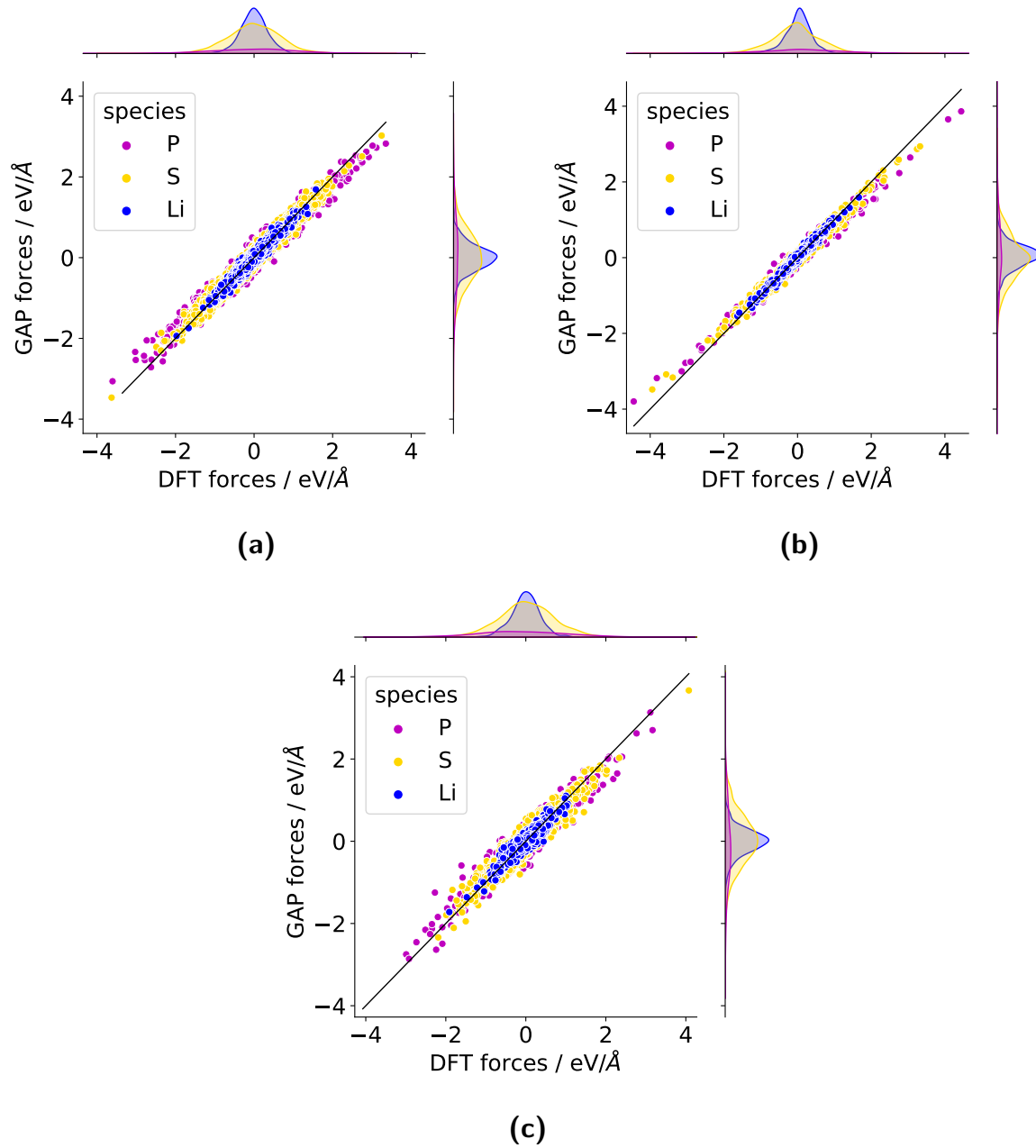


Figure 22: Force correlation plots for MD snapshots at 600 K of a) α -Li₃PS₄, b) γ -Li₃PS₄, and c) Li₇P₃S₁₁. Snapshots are extracted exclusively from MD runs at 600 K.

Table 6: Force and energy RMSEs for the three crystal phases used for validation. Force RMSEs of α - and γ - Li_3PS_4 crystals are comparable to the ones of the β phase, on which the model has been trained. An offset is observed between DFT energies and GAP predictions for all three crystal phases, however the relative energy prediction (reported in brackets and obtained by subtracting the observed energy offset) within the samples are comparable to those obtained for the β - Li_3PS_4 crystal.

Phase	Force RMSE / $\text{eV}/\text{\AA}$	Energy RMSE (corr) / meV/atom
α - Li_3PS_4	0.12	129 (1.4)
γ - Li_3PS_4	0.11	16 (2.0)
$\text{Li}_7\text{P}_3\text{S}_{11}$	0.19	22 (0.7)

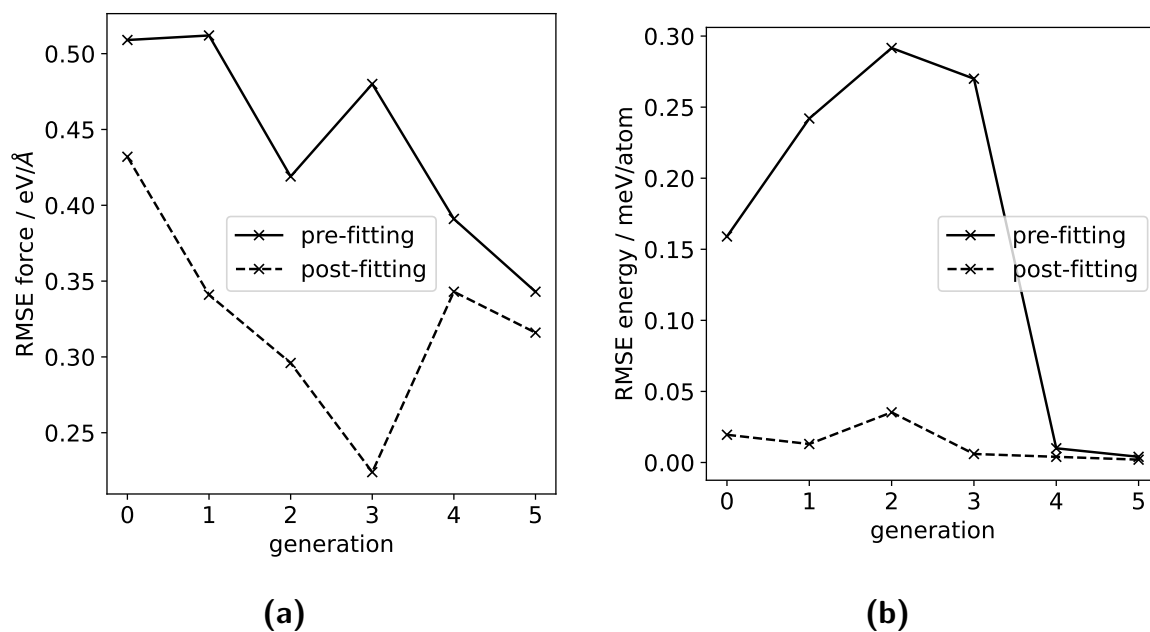


Figure 23: Obtained force (a) and energy errors (b) for the training steps necessary to incorporate the $\text{P}_2\text{S}_6^{4-}$ building block into the amorphous materials, as described in Section 5.4.

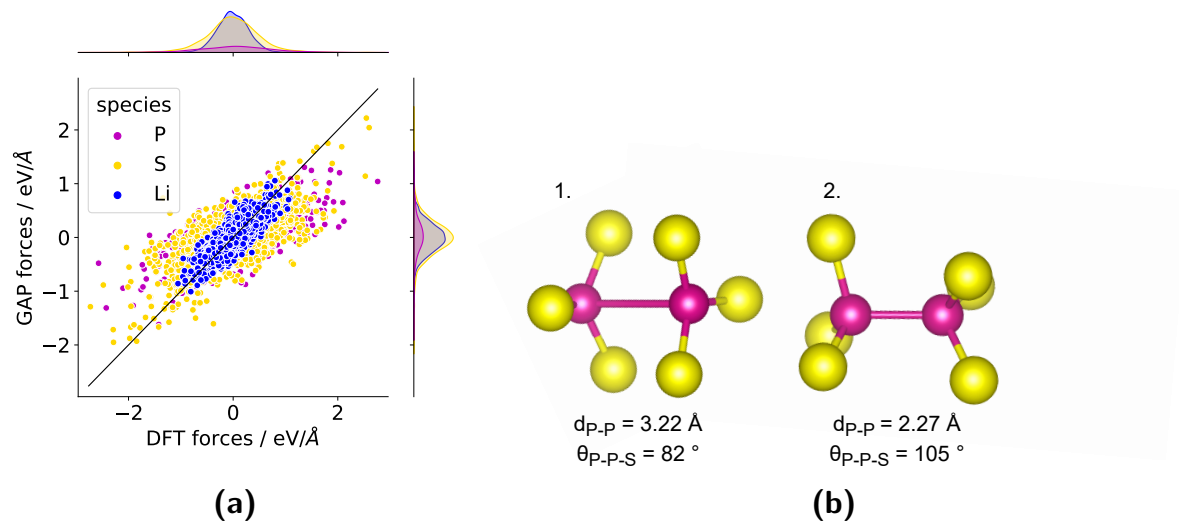


Figure 24: a) Force correlation plot for the last generation of FF training of a sampled glasses containing $P_2S_6^{4-}$ and PS_4^{3-} in a ratio of 1:1. b) Structure of the $P_2S_6^{4-}$ building block extracted from the $Li_4P_2S_6$ crystal (1) and from small DFT optimized glassy cells (2). Phosphorous is displayed in violet and sulfur in yellow.

8.2 Molecular Dynamics

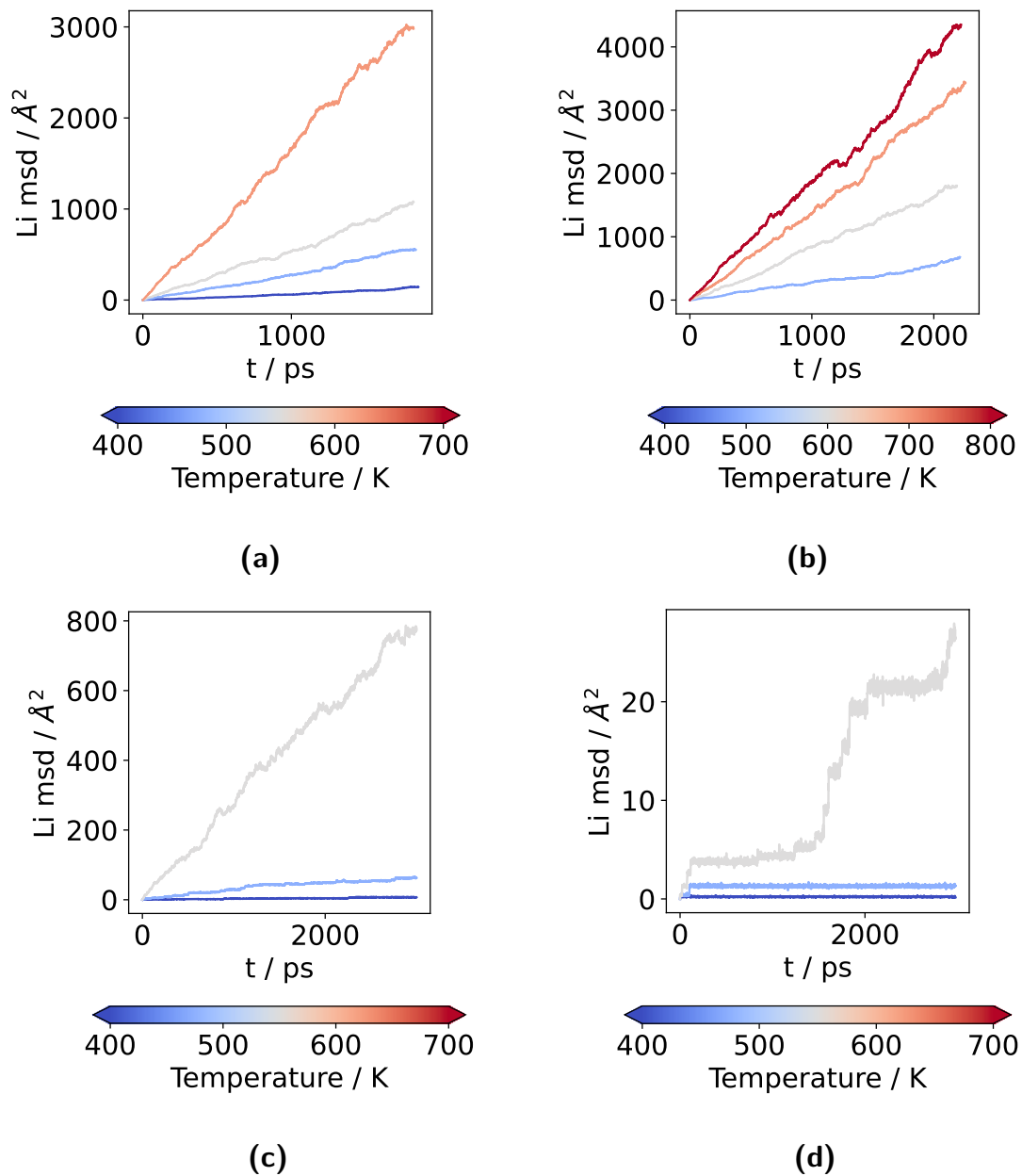


Figure 25: Li mean square displacements for MD runs of a) Li₇P₃S₁₁, b) α- c) β-, and d) γ-Li₃PS₄ crystals.

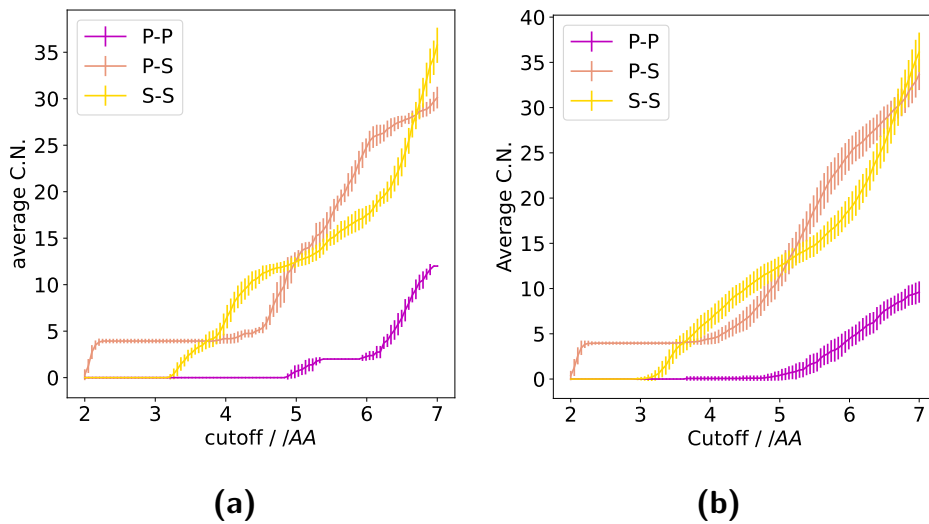


Figure 26: Coordination number for P-P, P-S and S-S bonds as a function of the imposed cutoff for a) β -Li₃PS₄ and b) Glass.

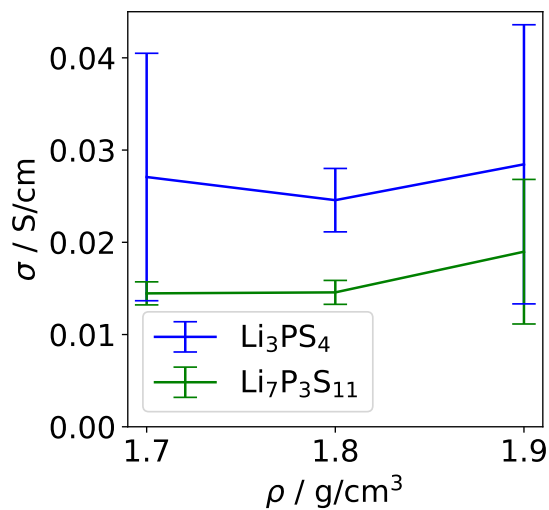


Figure 27: Density dependence of the conductivity of Li₃PS₄ and Li₇P₃S₁₁ glasses, using an ensemble of three structures for each density and stoichiometry.

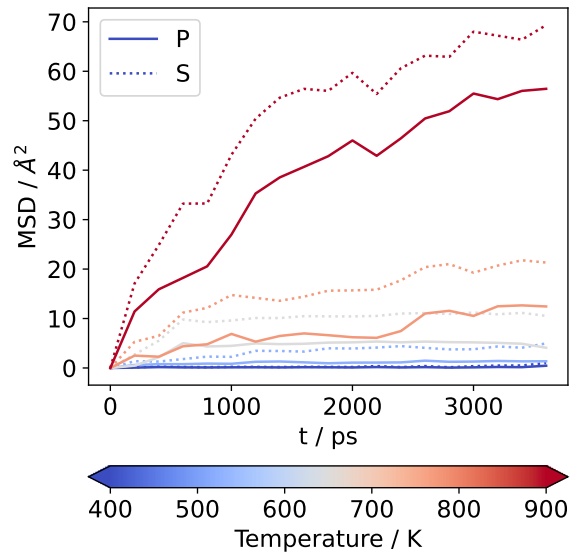


Figure 28: Mean square displacement of phosphorous and sulfur atoms as a function of different temperatures in Li_3PS_4 glasses with $\rho=1.8 \text{ g cm}^{-3}$. For temperatures below 600 K the mean square displacements converge after an initial equilibration period, which is not the case anymore for temperatures of 700 K and higher.

Table 7: Pearson coefficients for the correlation of the $\text{P}_2\text{S}_n^{4-}$ ($n = 6,7$) content in different LPS glasses and their corresponding lithium ion conductivity at $T = 400\text{--}700 \text{ K}$.

Stoichiometry	Temperature / K	Pearson correlation	P value
Li_3PS_4	400	-0.22	0.35
Li_3PS_4	500	-0.30	0.19
Li_3PS_4	600	-0.39	0.09
Li_3PS_4	700	0.06	0.79
$\text{Li}_7\text{P}_3\text{S}_{11}$	400	-0.21	0.38
$\text{Li}_7\text{P}_3\text{S}_{11}$	500	-0.24	0.32
$\text{Li}_7\text{P}_3\text{S}_{11}$	600	-0.21	0.38
$\text{Li}_7\text{P}_3\text{S}_{11}$	700	0.20	0.40
$\text{Li}_4\text{P}_2\text{S}_7$	400	-0.19	0.43
$\text{Li}_4\text{P}_2\text{S}_7$	500	0.02	0.93
$\text{Li}_4\text{P}_2\text{S}_7$	600	-0.17	0.47
$\text{Li}_4\text{P}_2\text{S}_7$	700	-0.48	0.03

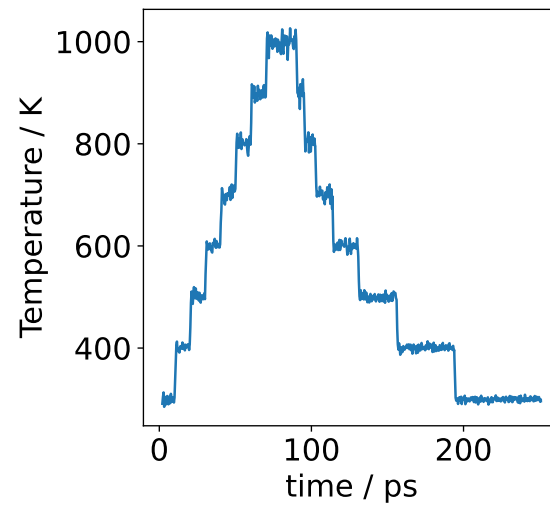


Figure 29: Employed sintering protocol for interface structures. After stepwise heating in 100 K steps to a temperature of 1000 K, a computational sintering-inspired stepwise cooling is performed which involves an increase of the equilibration time by a factor of 1.5 after every cooling step. The NVT ensemble is used throughout.

List of Figures

1	P-S microchemistry contained in the $x\text{Li}_2\text{S}-(100-x)\text{P}_2\text{S}_5$ material class. a) <i>ortho</i> -thiophosphate PS_4^{3-} , b) <i>pyro</i> -thiophosphate $\text{P}_2\text{S}_7^{4-}$, c) <i>hypo</i> -thiodiphosphate $\text{P}_2\text{S}_6^{4-}$, d) <i>meta</i> -thidiphosphate $\text{P}_2\text{S}_6^{2-}$, e) <i>meta</i> -thiophosphate chain $(\text{PS}_3^-)_n$. [3]. Phosphorous is displayed in violet, sulfur in yellow.	3
2	Crystal phases of Li_3PS_4 a) $\alpha\text{-Li}_3\text{PS}_4$ b) $\beta\text{-Li}_3\text{PS}_4$ c) $\gamma\text{-Li}_3\text{PS}_4$. The γ -phase is the stable one at room temperature, which exhibits a phase change to the β -phase at 500-700 K. Lithium is displayed in blue, phosphorous in violet, and sulfur in yellow.	4
3	Further crystal structures existing in the ternary Li-P-S system. a) The metastable $\text{Li}_7\text{P}_3\text{S}_{11}$ crystal, which contains in a ratio of 1:1 PS_4^{3-} and $\text{P}_2\text{S}_7^{4-}$ building blocks. b) $\text{Li}_4\text{P}_2\text{S}_6$, containing exclusively $\text{P}_2\text{S}_6^{4-}$ building blocks. Lithium is displayed in blue, phosphorous in violet, and sulfur in yellow.	5
4	a) Workflow for the iterative training approach of crystalline structures. Hot MD snapshots ($T = 600$ K) are added to the force field training set until a convergence of force and energy RMSEs is approached. b) Force correlation for the final validation set. c) Force RMSEs and d) Energy RMSEs for the iterative training. Final RMSEs are approximately 0.1 eV \AA^{-1} and 2.5 meV/atom	17
5	a) Workflow for the iterative training of amorphous LPS structures. b) Force correlation plot for the validation set of the last generation. c) Development of force error and d) energy error for training and validation set. Generation 0-2 corresponds to the sampling-based, generation 3-6 to the molecular dynamics-based training.	21
6	Systematic sampling of P-P distances in the $\text{Li}_4\text{P}_2\text{S}_6$ crystal. a) Geometries used for the sampling approach: The initial structure is distorted by displacing one phosphorous atom (i.e. shortening the P-P bond length). Lithium is displayed in blue, phosphorous in burple, sulfur in yellow, and the phosphorous atoms in the distorted structures in light grey. b) Obtained energy profile from DFT, untrained, and trained GAP as a function of P-P distance.	23
7	Coordination-resolved force correlation plot for P (a), and S (b) atoms in MD snapshots of $\text{Li}_7\text{P}_3\text{S}_{11}$ glasses.	24
8	Convergence behavior of the force field during GAP-RSS for a) atomic forces and b) atomic energies.	26
9	Force RMSEs of glass, crystal and AIRSS training set for different AIRSS conditions.	27

10	a) Violin plot comparing the energy distribution of RSS structures (GAP-RSS and AIRSS) to structures already in the training set (MD snapshots at 600 K from the β -crystal and the Li_3PS_4 amorphous structure). b) kPCA decomposition of local SOAP descriptors, comparing the same structures as in a). Lithium is indicated by triangles, sulfur by crosses and phosphorous by rhombs.	28
11	Computational Arrhenius plots for a) $\text{Li}_7\text{P}_3\text{S}_{11}$ and b) α , β and γ phase of Li_3PS_4 . Good correlations are found for $\text{Li}_7\text{P}_3\text{S}_{11}$. A phase transition to the α -phase explains the step in conductivity for β - and γ - Li_3PS_4 between 600 and 700 K.	31
12	S-S RDFs for MD snapshots of a) β - Li_3PS_4 and b) γ - Li_3PS_4 at different temperatures. The disappearing of the peak at 4.3 Å, occurring for both structures at 700 K, proves the phase transition to the α -phase.	32
13	Radial distribution functions for a) P-S, b) S-Li, c) S-S and d) P-P, collected from molecular dynamics runs of α , β , and γ -crystals at 500K, using an averaged ensemble of 20 different Li_3PS_4 glasses with $\rho = 1.8 \text{ g cm}^{-3}$.	36
14	Average building block compositions for different MD temperatures, displayed for a) Li_3PS_4 , b) $\text{Li}_7\text{P}_3\text{S}_{11}$, and c) $\text{Li}_4\text{P}_2\text{S}_7$.	37
15	Conductivity as a function of $\text{P}_2\text{S}_n^{4-}$ ($n = 6,7$) content in the glassy structure for a) Li_3PS_4 , b) $\text{Li}_7\text{P}_3\text{S}_{11}$, and c) $\text{Li}_4\text{P}_2\text{S}_7$. No correlation is observed for any combination of stoichiometry and temperature.	38
16	Arrhenius plot for the three glass stoichiometries, using an ensemble of 20 structures for each temperature and MD runs of 1.5 ns length. It is found that all glasses have alike activation barriers for diffusion.	39
17	Interface model for β - Li_3PS_4 and the (110)-surface termination a) before equilibration and b) after equilibration. Lithium is displayed in blue, phosphorous in violet, and sulfur in yellow.	42
18	Degree of amorphization across the interface coordinate for a) (100), b) (010), c) (001) and d) ($\bar{1}10$) interfaces, probing an ensemble of three structures for every surface index (displayed in blue, green and red). For all surfaces, the boundary regions are marked with dotted lines. The width of the interfacial regions is approximately 7 Å, independent of surface termination.	43
19	Region-resolved P-P (a) and S-S (b) radial distribution functions of the interface structure. The functions are averaged over interfaces of all four examined surface orientations, as they do not exhibit significant differences.	44
20	kPCA plots of SOAP dissimilarity for phosphorous (a) and sulfur (b), highlighting that there is no fundamental structural difference of the interface from the glass- and crystalline structures.	45

21	Lithium MSD for glass, crystal, and interfacial region in comparison to the MSDs of β -Li ₃ PS ₄ and amorphous Li ₃ PS ₄ . Trajectories from interfaces with all previously mentioned surface terminations are shown.	46
22	Force correlation plots for MD snapshots at 600 K of a) α -Li ₃ PS ₄ , b) γ -Li ₃ PS ₄ , and c) Li ₇ P ₃ S ₁₁ . Snapshots are extracted exclusively from MD runs at 600 K. .	49
23	Obtained force (a) and energy errors (b) for the training steps necessary to incorporate the P ₂ S ₆ ⁴⁻ building block into the amorphous materials, as described in Section 5.4.	50
24	a) Force correlation plot for the last generation of FF training of a sampled glasses containing P ₂ S ₆ ⁴⁻ and PS ₄ ³⁻ in a ratio of 1:1. b) Structure of the P ₂ S ₆ ⁴⁻ building block extracted from the Li ₄ P ₂ S ₆ crystal (1) and from small DFT optimized glassy cells (2). Phosphorous is displayed in violet and sulfur in yellow.	51
25	Li mean square displacements for MD runs of a) Li ₇ P ₃ S ₁₁ , b) α - c) β -, and d) γ -Li ₃ PS ₄ crystals.	52
26	Coordination number for P-P, P-S and S-S bonds as a function of the imposed cutoff for a) β -Li ₃ PS ₄ and b) Glass.	53
27	Density dependence of the conductivity of Li ₃ PS ₄ and Li ₇ P ₃ S ₁₁ glasses, using an ensemble of three structures for each density and stoichiometry.	53
28	Mean square displacement of phosphorous and sulfur atoms as a function of different temperatures in Li ₃ PS ₄ glasses with $\rho=1.8$ g cm ⁻¹ . For temperatures below 600 K the mean square displacements converge after an initial equilibration period, which is not the case anymore for temperatures of 700 K and higher.	54
29	Employed sintering protocol for interface structures. After stepwise heating in 100 K steps to a temperature of 1000 K, a computational sintering-inspired stepwise cooling is performed which involves an increase of the equilibration time by a factor of 1.5 after every cooling step. The NVT ensemble is used throughout.	55

List of Schemes

1	Summarized properties which are demanded for metrics describing chemical environments: Additivity, invariance with respect to rotation, translation and permutation, completeness and smoothness. Reprinted with permission from Deringer <i>et al.</i> [29] Copyright 2021 American Chemical Society.	10
---	--	----

- 2 Graphical representation of the sampling approach, involving random sampling of thiophosphate compounds on a predefined grid, addition of lithium ions via a Voronoi Tessellation of the anion grid, and iterative compressing to the desired density. Lithium is displayed in blue, phosphorous in violet, and sulfur in yellow 20

References

- [1] J. Janek, W. G. Zeier, *Nat. Energy* **2016**, *1*.
- [2] A. L. Robinson, J. Janek, *MRS Bulletin* **2014**, *39*, 1046–1047.
- [3] Ömer Ulaş Kudu et al., *J Power Sources* **2018**, *407*.
- [4] N. Kamaya et al., *Nat. Mater.* **2011**, *10*, 682–686.
- [5] H. Aono et al., *J Electrochem Soc* **1990**, *137*, 1023–1027.
- [6] M Tachez et al., *Solid State Ionics* **1984**, *14*, 181–185.
- [7] Y. Yang et al., *ACS Applied Materials & Interfaces* **2016**, *8*, 25229–25242.
- [8] T. Baba, Y. Kawamura, *Front. Energy Res.* **2016**, *4*.
- [9] J.-S. Kim et al., *The Journal of Physical Chemistry Letters* **2018**, *9*, 5592–5597.
- [10] Z. Liu et al., *J. Am. Chem. Soc.* **2013**, *135*, 975–978.
- [11] S. Wenzel et al., *Solid State Ionics* **2016**, *286*, 24–33.
- [12] M. R. Busche et al., *Chem Mater* **2016**, *28*, 6152–6165.
- [13] H Yamane et al., *Solid State Ionics* **2007**, *178*, 1163–1167.
- [14] K. Minami et al., *J. Am. Ceram. Soc.* **2011**, *94*, 1779–1783.
- [15] H. Tsukasaki et al., *Sci. Rep.* **2017**, *7*.
- [16] C. Dietrich et al., *J. Mater. Chem.A* **2017**, *5*, 18111–18119.
- [17] J.-S. Kim et al., *ACS Applied Materials & Interfaces* **2018**, *11*, 13–18.
- [18] K. Homma et al., *Solid State Ionics* **2011**, *182*, 53–58.
- [19] M Murayama et al., *Solid State Ionics* **2004**, *170*, 173–180.
- [20] S. Shiotani et al., *Sci. Rep.* **2017**, *7*.
- [21] Z. D. Hood et al., *Solid State Ionics* **2016**, *284*, 61–70.
- [22] Y. Seino et al., *Energy Environ. Sci.* **2014**, *7*, 627–631.
- [23] I.-H. Chu et al., *ACS Applied Materials & Interfaces* **2016**, *8*, 7843–7853.
- [24] M. B. Preefer et al., *ACS Applied Materials & Interfaces* **2021**, *13*, 57567–57575.
- [25] K. Ohara et al., *Sci. Rep.* **2016**, *6*.
- [26] J. G. Smith, D. J. Siegel, *Nat Commun* **2020**, *11*.
- [27] Y. Seino et al., *J. Mater. Chem.A* **2015**, *3*, 2756–2761.
- [28] N. H. H. Phuc et al., *Solid State Ionics* **2016**, *288*, 240–243.
- [29] V. L. Deringer et al., **2021**, *121*, 10073–10141.

- [30] F. Musil et al., *Chem. Rev.* **2021**, *121*, 9759–9815.
- [31] R. Jinnouchi et al., *J. Chem. Phys.* **2020**, *152*, 234102.
- [32] A. P. Bartók et al., *Phys. Rev. B* **2013**, *87*, 184115.
- [33] The QUIP atomistic simulation software package is available from <https://github.com/libAtoms/QUIP>.
- [34] A. P. Bartók et al., *Phys. Rev. Lett.* **2010**, *104*, 136403.
- [35] J. Mavračić et al., **2018**, *9*, 2985–2990.
- [36] S. De et al., *Phys. Chem. Chem. Phys.* **2016**, *18*, 13754–13769.
- [37] B. Schölkopf et al., *Neural Comput.* **1998**, *10*, 1299–1319.
- [38] V. Blum et al., *Comput. Phys. Commun.* **2009**, *180*, 2175–2196.
- [39] J. P. Perdew et al., *Phys. Rev. Lett.* **1996**, *77*, 3865–3868.
- [40] A. Jain et al., *APL Materials* **2013**, *1*, 011002.
- [41] S. Plimpton, *J. Comput. Phys.* **1995**, *117*, 1–19.
- [42] S. Nosé, *J. Chem. Phys.* **1984**, *81*, 511–519.
- [43] A. H. Larsen et al., *J. Phys.: Condens. Matter* **2017**, *29*, 273002.
- [44] C. Barber, H. Huhdanpaa, URL: <http://www.geom.umn.edu/software/qhull>.
- [45] J. MacQueen et al. in Proceedings of the fifth Berkeley symposium on mathematical statistics and probability, Vol. 1, Oakland, CA, USA, **1967**, pp. 281–297.
- [46] S. Stegmaier et al., *Adv. Energy Mater.* **2021**, *11*, 2100707.
- [47] K. Momma, F. Izumi, VESTA: a Three-Dimensional Visualization System for Electronic and Structural Analysis, **2013**.
- [48] L. Himanen et al., *Computer Physics Communications* **2020**, *247*, 106949.
- [49] C. J. Pickard, R. J. Needs, *J. Phys.: Condens. Matter* **2011**, *23*, 053201.
- [50] T. Huss, “Molecular dynamics based sampling of $x(\text{Li}_2\text{S})-(100-x)\text{P}_2\text{S}_5$ glasses”, Research internship, **2020**.
- [51] C. G. Staacke et al., *ACS Applied Energy Materials* **2021**, *4*, 12562–12569.
- [52] A. Sakuda et al., *J. Ceram. Soc. Jpn.* **2013**, *121*, 946–949.
- [53] V. L. Deringer et al., *Faraday Discuss.* **2018**, *211*, 45–59.
- [54] F. H. Stillinger, *Phys. Rev. E* **1999**, *59*, 48–51.
- [55] H. M. Senn, W. Thiel, *Angewandte Chemie International Edition* **2009**, *48*, 1198–1229.
- [56] D. Berger et al., *The Journal of Chemical Physics* **2014**, *141*, 024105.

-
- [57] I. Goodfellow et al., *Advances in neural information processing systems* **2014**, 27.
- [58] D. Frenkel, B. Smit in *Understanding Molecular Simulation (Second Edition)*, (Eds.: D. Frenkel, B. Smit), Academic Press, San Diego, **2002**, pp. 63–107.
- [59] H. H. Heenen, Dissertation, Technische Universität München, München, **2018**.
- [60] N. J. de Klerk et al., *ACS Applied Energy Materials* **2018**, 1, 3230–3242.
- [61] R. Garcia-Mendez et al., *Adv. Energy Mater.* **2020**, 10, 2000335.
- [62] A. Hayashi et al., *J. Non-Cryst. Solids* **2010**, 356, 2670–2673.
- [63] A. Hayashi et al., *J. Am. Ceram. Soc.* **2004**, 84, 477–79.
- [64] M. A. Caro, *Phys. Rev. B* **2019**, 100, 024112.
- [65] C. Staacke et al., **2021**, DOI 10.26434/chemrxiv-2021-73w0p.